The Astrophysical Journal Letters, 970:L4 (18pp), 2024 July 20 https://doi.org/10.3847/2041-8213/ad5c6c

Updated Spectral Characteristics for the Ultracool Dwarf TRAPPIST-1

Fatemeh Davoudi[1], Benjamin V. Rackham[2,3,7], Michaël Gillon[1], Julien de Wit[2], Adam J. Burgasser[4], Laetitia Delrez[1], Aishwarya Iyer[5,8], and Elsa Ducrot[1,6]
[1] Astrobiology Research Unit, Université de Liège, Allée du 6 Août 19C, B-4000 Liège, Belgium; Fatemeh.Davoudi@uliege.be
[2] Department of Earth, Atmospheric and Planetary Science, Massachusetts Institute of Technology, 77 Massachusetts Avenue, Cambridge, MA 02139, USA
[3] Kavli Institute for Astrophysics and Space Research, Massachusetts Institute of Technology, Cambridge, MA 02139, USA
[4] Department of Astronomy & Astrophysics, University of California, San Diego, La Jolla, CA 92093, USA
[5] Goddard Space Flight Center, 8800 Greenbelt Rd., Greenbelt, MD 20771, USA
[6] LESIA, Observatoire de Paris, CNRS, Université Paris Diderot, Université Pierre et Marie Curie, 5 place Jules Janssen, 92190 Meudon, France
Received 2024 May 12; revised 2024 June 22; accepted 2024 June 24; published 2024 July 11

Abstract

A comprehensive infrared spectroscopic study of star TRAPPIST-1 is a crucial step toward the detailed examination of its planets. While the presence of Earth's atmosphere has limited the spectral extent of such a study up to now, the Near Infrared Imager and Slitless Spectrograph (NIRISS) and the Near Infrared Spectrograph instruments aboard the James Webb Space Telescope (JWST) can now yield the 0.6–5 μm spectral energy distribution (SED) of the star. Here we translate TRAPPIST-1's SED into tight constraints on its luminosity ($L_{\rm bol} = 0.000566 \pm 0.000022\ L_{\odot}$), effective temperature ($T_{\rm eff} = 2569 \pm 28$ K), and metallicity ([Fe/H] $= 0.052 \pm 0.073$) and investigate the behavior of its gravity-sensitive indices. Through band-by-band comparisons of the NIRISS and ground-based spectra, TRAPPIST-1 exhibits a blend of both field source and intermediate-gravity spectral characteristics, suggesting that the star is likely a field-age source with spectral features reminiscent of young objects. We also employ photospheric modeling incorporating theoretical and JWST spectra to constrain stellar surface heterogeneities, finding that the limited fidelity of current stellar spectral models precludes definitive constraints on the physical parameters of the distinct spectral components giving rise to TRAPPIST-1's photospheric heterogeneity and variability. In addition, we find intermodel differences in the inferences of properties (e.g., the effective temperature) over one order of magnitude larger than the instrument-driven uncertainties (∼100 K vs. ∼4 K), pointing toward a model-driven accuracy wall. Our findings call for a new generation of stellar models to support the optimal mining of JWST data and further constraining stellar—and ultimately planetary—properties.

Unified Astronomy Thesaurus concepts: Exoplanets (498); M dwarf stars (982); Exoplanet systems (484)

1. Introduction

M dwarf stars ($0.08\ M_{\odot} < M_{*} < 0.6\ M_{\odot}$; Delfosse et al. 2000) compose approximately 73% of all stars (Dole 1964; Engle & Guinan 2011). At their low-mass end are ultracool M dwarfs with masses $M_{*} \leqslant 0.1\ M_{\odot}$ and effective temperatures $T_{\rm eff} \leqslant 3000$ K (Kirkpatrick et al. 1997; Maas et al. 2022). Among these, TRAPPIST-1 at 12.467 ± 0.011 pc (Gaia Collaboration et al. 2023) stands out as the most well-known specimen, featuring a unique system of seven temperate Earth-sized planets (Gillon et al. 2016, 2017). TRAPPIST-1 has a radius only slightly larger than that of Jupiter, has a surface temperature of around 2500 K (Gillon et al. 2016), and falls under the M8.0 ± 0.5 spectral class (Gillon et al. 2016). According to Brady et al. (2023), the expected rotation period of TRAPPIST-1 is approximately 2.9 ± 0.5 days, based on the star's projected rotation velocity of $2.1 \pm 0.3\ {\rm km\ s^{-1}}$. This aligns with the 3.3-day semiperiodic signal found in Kepler photometry (Roettenbacher & Kane 2017; Luger et al. 2017; Vida et al. 2017).

TRAPPIST-1 was described by Gillon et al. (2016, and references therein) as a moderately active star with an estimated surface magnetic field strength of around 600^{+200}_{-400} G over its surface (Reiners & Basri 2010). The customary consequence of magnetic activity is variations in the configurations of the host star's spectral line profiles (e.g., Desort et al. 2007; Reiners & Basri 2010; Barnes et al. 2014; Jeffers et al. 2018). Such profile variations align with the timescales of the specific activity characteristics, from several seconds to extended periods of several years (Burgasser & Mamajek 2017; Jeffers et al. 2018). In this context, TRAPPIST-1 consistently exhibits the presence of Hα emission in its spectrum at a level of $L_{\rm H\alpha}/L_{\rm bol} = (2.5\text{–}4) \times 10^{-5}$ (Reiners & Basri 2010; Burgasser et al. 2015; Wheatley et al. 2017). Additionally, the star was shown to be an X-ray and ultraviolet (XUV) emitter, with a total XUV emission in the range $L_{\rm XUV}/L_{\rm bol} = (6\text{–}9) \times 10^{-4}$ from XMM observations (Wheatley et al. 2017) and a mean high-energy luminosity estimated to be $\log_{10}(L_{\rm XUV}/L_{\rm bol}) = -3.51$ via the Hubble Space Telescope (HST) observations (Bourrier et al. 2017).

TRAPPIST-1 exhibits strong flares in the XUV and optical (e.g., Gillon et al. 2016; Vida et al. 2017; Paudel et al. 2018). Flares with energies over 10^{29} erg happen about once every 2–3 days, whereas superflares with energies above 10^{33} erg happen roughly once every 3 months (Paudel et al. 2019). Lim et al. (2023) also revealed miniflares during transit observations obtained with JWST/Near Infrared Imager and Slitless Spectrograph (NIRISS). However, Burgasser & Mamajek (2017) found that, based on some measures, TRAPPIST-1 is less active than other M8 dwarfs. In contrast, Dmitrienko & Savanov (2018) estimated that spots cover 5% of the star's surface. This estimate was derived from the analysis of 21 K2

[7] 51 Pegasi b Fellow.
[8] NASA Postdoctoral Fellow.

Table 1
Summary of the Observations Used in This Study

Observation	P.I.	Program ID	Observation Date	SNR (pixel^{-1})	Resolving Power
UVES 1	A. Reiners	081.D-0190	2008-06-20	7	34540
UVES 2	J. Barnes	089.C-0904	2012-07-23	6.6	51690
UVES 3	J. Barnes	089.C-0904	2012-07-24	5.6	51690
UVES 4	J. Barnes	089.C-0904	2012-07-26	5.2	51690
UVES 5	J. Barnes	089.C-0904	2012-07-29	6.1	51690
SpeX+MagE	A. Burgasser	⋯	2009-08-27/2015-11-18	60	4100
NIRISS	O. Lim	2589	2022-07-18	323	700
NIRSpec	K. Stevenson	1981	2023-12-11	275	100

observational data sets, each covering one stellar rotation period, and involved constructing a map of the star's temperature inhomogeneities (Dmitrienko & Savanov 2018). Furthermore, Mullan et al. (2018) also constructed evolutionary models of TRAPPIST-1 that enable them to predict the vertical component of the surface magnetic field of TRAPPIST-1 to be in the range ∼1450–1700 G, higher than previous estimates (Reiners & Basri 2010). They suggested that the discrepancy might arise owing to the use of different line-fitting methods and noted that applying the approach outlined by Shulyak et al. (2017) for measuring the magnetic field of TRAPPIST-1 could lead to an increase in the field strength from the previously reported 600 G (Reiners & Basri 2010) to around 1400 G. This assumption is based on the idea that the magnetic field is dominated by its vertical component (Shulyak et al. 2017; Mullan et al. 2018).

In addition to the contradictions that exist regarding the level of magnetic activity, despite many efforts to refine TRAPPIST-1's physical properties (Howell et al. 2016; Gillon et al. 2016; Luger et al. 2017; Van Grootel et al. 2018; Paudel et al. 2019; Gonzales et al. 2019), the extraction of stellar parameters from its spectrum remains challenging. Indeed, an exact study of the star's photospheric structure and chromospheric activities related to its spectrum is needed. Moreover, active stars can produce significant levels of stellar contamination in precise transmission spectra of their planets (Rackham et al. 2018; Rackham et al. 2019). This stellar contamination originates from the nonhomogeneity of the stellar photosphere. In this context, the chord transited by a given planet may not be representative of the average stellar disk, resulting in signals in the transit transmission spectrum that can overwhelm the planetary signals by as much as an order of magnitude. As a result, failing to take stellar contamination into account can result in noticeable biases in transit transmission spectroscopy results (e.g., Pont et al. 2008; Iyer & Line 2020; Rackham & de Wit 2023).

Given these complexities, this study endeavors to contribute to a more nuanced understanding of TRAPPIST-1 by meticulously analyzing its spectral energy distribution (SED) and magnetic activity. In this context, we present a new characterization of TRAPPIST-1 properties through the analysis of medium-resolution infrared (IR) spectra gathered by the JWST instruments NIRISS and Near Infrared Spectrograph (NIRSpec), as well as moderate-to-high-resolution optical and IR spectra obtained with ground-based telescopes.

The Letter is structured as follows: Section 2 describes the data and its reduction, Section 3 presents a summary of the spectral analysis process and measurements, Section 4 focuses on stellar contamination, Section 5 presents an updated SED of the star, and Section 6 discusses our findings.

2. Data

In this analysis, we used five high-resolution spectra taken by the UVES spectrograph installed at the Nasmyth focus of Kueyen, Unit Telescope 2 of the Very Large Telescope array (Dekker et al. 2000). The calibrated data for these spectra were acquired from Phase 3 of the ESO archive science portal,[9] publicly available under the program IDs 081.D-0190 and 089.C-0904, with principal investigators A. Reiners and J. Barnes. We employed them to extend the coverage of the Hα line across a broader spectral range. The details of these observations, which cover wavelengths from 650 nm to around 1025 nm with a signal-to-noise ratio (SNR) of more than 5.2 pixel^{-1}, along with other observations, are given in Table 1.

Additionally, a combined spectrum was used, created by merging spectroscopy data from two distinct observations. The integration of two spectra (ranging from 0.6 to 0.9 μm and from 0.9 to 2.5 μm, respectively) resulted in a unified spectrum spanning from 0.6 to 2.5 μm. We refer to this spectrum as SpeX+MagE in Table 1. One spectrum was acquired using the short-wavelength cross-dispersed (SXD) mode of the IRTF/SpeX instrument on the 3 m NASA Infrared Telescope Facility (Rayner et al. 2003), while the other was obtained with the Magellan Echellette (MagE) Spectrograph on the 6.5 m Magellan Clay Telescope at Las Campanas Observatory (Marshall et al. 2008).

The SpeX-SXD data, collected in the near-IR spectrum on 2015 November 18, within the *K* band, were previously published by Gillon et al. (2016). Meanwhile, the spectrum observed using the Magellan/MagE spectrograph on 2009 August 27 was utilized in the analysis of Burgasser et al. (2015). The merged spectrum was reduced using the `Spextool` package version 4.04 (Vacca et al. 2003; Cushing et al. 2005), corrected for telluric absorption, and calibrated to absolute (erg s^{-1} cm^{-2} μm^{-1}) using its absolute Two Micron All Sky Survey (2MASS) *J* magnitude. Data reduction involved flat-field correction, wavelength calibration, optimal source extraction, and flux calibration.

Finally, we used publicly available spectra of TRAPPIST-1 taken by the NIRISS (Doyon et al. 2023) and NIRSpec (Jakobsen et al. 2022) instruments aboard the JWST. The NIRISS data for this study include a medium-resolution spectrum ($R \approx 700$) taken on 2022 July 18, using the Clear GR700XD filter in the single object slitless spectroscopy (SOSS) mode (Albert et al. 2023). This spectrum spans the wavelength range of 0.6–2.8 μm and was taken under the program JWST GO-2589 (PI: O. Lim; Lim et al. 2023). The observation windows for this observation were carefully chosen to minimize contamination from field stars, given the instrument's slitless

[9] *ESO Archive Science Portal*

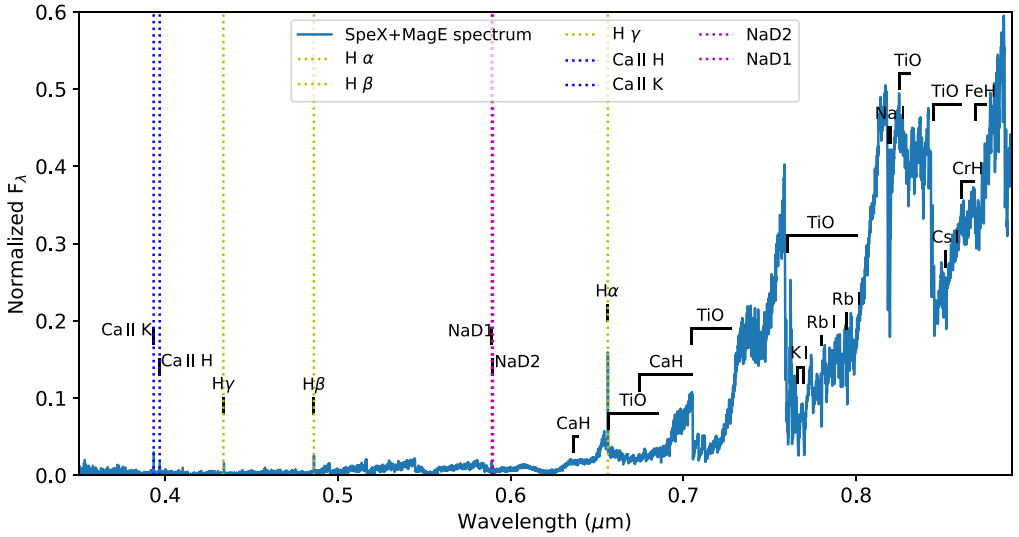

Figure 1. Positions of significant atomic lines and molecular bands in the SpeX+MagE spectrum (0.3–0.9 μm). The emission lines and molecules that are predominantly responsible for certain absorption features are indicated at the relevant wavelengths.

nature (Lim et al. 2023). The data were processed using three distinct pipelines: `supreme-SPOON` (Feinstein et al. 2023; Coulombe et al. 2023; Radica et al. 2023), `NAMELESS` (Feinstein et al. 2023; Coulombe et al. 2023), and `SOSSISSE` (Albert et al. 2023). This redundancy was employed to validate the consistency of the results. For more information about the `supreme-SPOON` and `NAMELESS` pipelines, refer to Appendix A in Lim et al. (2023). We utilized the high-SNR spectrum produced by combining all out-of-transit spectra gathered for a single visit, as obtained by Lim et al. (2023) and made available for this study. The median of the out-of-transit stellar spectrum consists of flux and its uncertainties measured in Jy, along with wavelength data in microns. The flux and flux uncertainties were converted from Jy to erg s^{-1} cm^{-2} $Å^{-1}$ for comparison to stellar spectral models.

Additionally, a low-resolution spectrum ($R \approx 100$) within the range of 0.6–5.3 μm was used, which was observed by NIRSpec in PRISM mode on 2023 December 11, under program ID 1981. We downloaded the fully calibrated product (_x1dints file) of NIRSpec from the Space Telescope Science Institute (STScI) portal,[10] which was extracted by the JWST Science Calibration Pipeline stage 3. The data had undergone standard processing with calibration version 1.8.2 and data processing version 2022_4a, using JWST version 1.11.4 (Bushouse et al. 2023) and CRDS version 11.16.16 with the "jwst_0421.pmap" CRDS context. We derived a high-SNR corrected mean spectrum by combining all 1D spectra of the _x1dints file using the `Jwst.combine_1d` function. This function computes a weighted average of 1D spectra, including wavelength and calibrated flux, as well as flux uncertainty. We integrated the flux over the entire wavelength range, converting the flux from frequency units (MJy) to wavelength units (erg s^{-1} cm^{-2} $Å^{-1}$). Since this observation was targeting the transit of TRAPPIST-1 h and included a transit of TRAPPIST-1 b in the middle of the transit of TRAPPIST-1 h at that time, we removed both transits using their transit time information and transformed this spectrum into the mean of the out-of-transit integrations.

[10] *STScI Portal*

3. Photospheric and Chromospheric Spectral Features

We started our analysis by identifying the positions of absorption and emission lines, as well as absorption bands, present in our TRAPPIST-1 spectra. We used the `SPLAT` Python package (Schneider et al. 2016; Burgasser & Splat Development Team 2017) to measure these lines in data from the NIRISS, UVES, and SpeX+MagE spectra. Consistent with previous studies (e.g., Burgasser et al. 2015; Burgasser & Mamajek 2017), the spectra exhibit the prominent features typical of the spectra of late M stars, such as absorption from water (H_2O) at about 0.9–2.2 μm (Polyansky et al. 2018); metal hydrides like FeH (head at 0.99 μm), CaH, and CrH; and metal oxides such as TiO, vanadium oxide (VO), and first CO overtone bands in the K band at 2.3 μm (Cushing et al. 2003; Rayner et al. 2009; Gharib-Nezhad & Line 2019; Gharib-Nezhad et al. 2021), which are depicted in Figures 1, 2, and 3. Absorption bands of TiO and VO in the photosphere might cover several spectral band heads over the 0.82–1.5 μm range and become combined with other spectral indices in the red–optical spectra of mid-to-late-type M stars (e.g., Kirkpatrick et al. 1991; Cushing et al. 2005; Rayner et al. 2009; Schöfer et al. 2019).

We labeled neutral alkali lines like Ca I, K I, Na I, Cs I, and Rb I, along with ionized lines like Ca II, all of which are identified in Figure 1, namely the Na I doublets at 0.82, 1.14, and 2.20 μm and the K I doublets at 0.77, 1.17, and 1.25 μm. Moreover, emission lines, as identified by the vertical dotted lines in Figures 1 and 3 across the SpeX+MagE and NIRISS spectra, will be discussed in detail in Section 3.3.

3.1. Metallicity Indicators in the NIRISS Data

Rojas-Ayala et al. (2010) established that M dwarf metallicities can be estimated by analyzing the absorption lines of 2.205 μm Na I and 2.263 μm Ca I. Gillon et al. (2016) applied this method to TRAPPIST-1, determining its [Fe/H] from the equivalent widths (EW) of these features in the reduced near-IR SpeX spectrum. They used the H_2O–K2 index and the mid- and late M dwarf metallicity calibration provided by Mann et al. (2014) to find [Fe/H] $= 0.040 \pm 0.080$ dex.

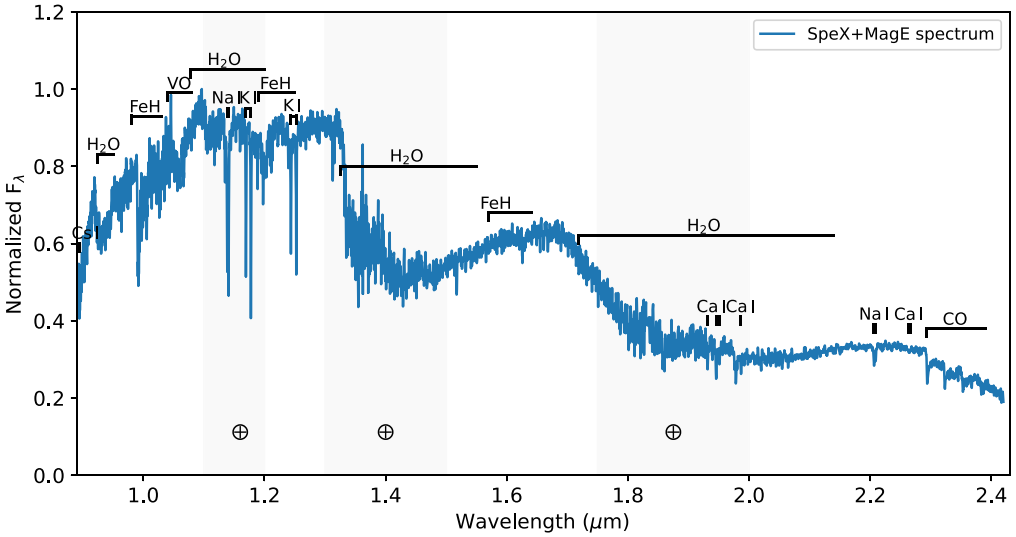

Figure 2. Positions of significant atomic lines and molecular bands in the SpeX+MagE spectrum (0.9–2.4 μm). Some spectral regions with high telluric contamination are shaded.

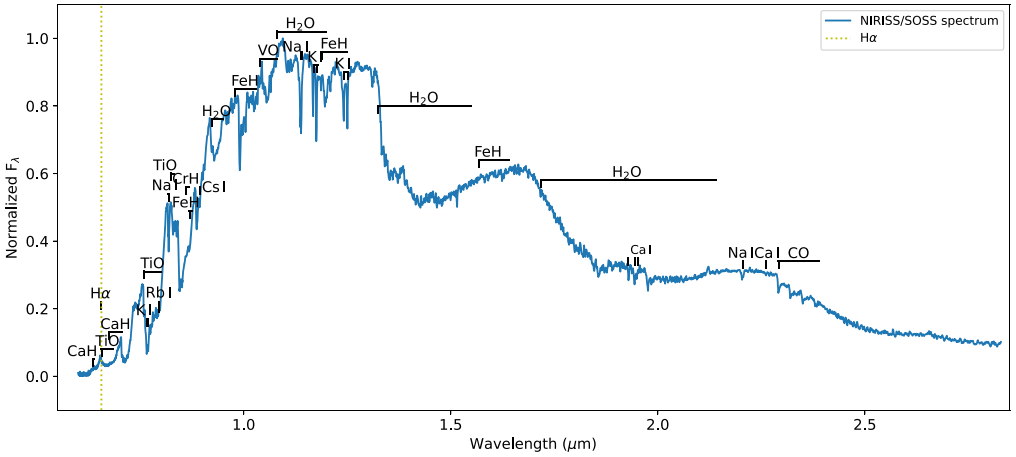

Figure 3. Positions of significant atomic lines and molecular bands in the NIRISS spectrum (0.6–2.8 μm).

We employed the same methodology as Gillon et al. (2016), but using metallicity indicators present in the NIRISS spectrum instead of the SpeX spectrum, as Ca I and Na I lines are labeled between 2.17 and 2.35 μm in Figure 3. In our measurements, we computed the EWs of the Na I doublet as 4.429 ± 0.063 and those of the Ca I doublet as 1.180 ± 0.065. The standard definition of the EW of a line is expressed as (Rojas-Ayala et al. 2012)

$$\mathrm{EW}_\lambda = \int_{\lambda_1}^{\lambda_2} \left(1 - \frac{F(\lambda)}{F_c(\lambda)}\right) d\lambda, \quad (1)$$

where $F(\lambda)$ represents the flux over the wavelength range of the line ($\lambda_2 - \lambda_1$) and $F_c(\lambda)$ signifies the estimated continuum flux on either side of the absorption feature. To estimate the uncertainties on the EW measurements, we applied a Monte Carlo approach by generating random samples for the flux and continuum flux at each wavelength point. These samples were drawn from normal distributions reflecting the measured flux uncertainties. Additionally, we used the `equivalent-width` function available in the `Specutils` Python package (Astropy-Specutils Development Team 2019), which yields consistent results. Then, we calculated the H_2O–K2 index to be 0.069 ± 0.003 by applying the mid- and late M dwarf metallicity calibration provided by Mann et al. (2014). Subsequently, we determined the [Fe/H] to be 0.052 ± 0.073. Metallicity uncertainty was estimated using a Monte Carlo approach (see Delrez et al. 2022). Therefore, the NIRISS spectra yielded a metallicity estimate consistent with previous findings, and it is subject to similar uncertainties. We note that the systematic uncertainty with this calibration, 0.07 dex, dominates the total uncertainty budget of our estimate.

3.2. Gravity Indicators in the NIRISS Data

At lower gravity, the photosphere experiences lower pressure, leading to noticeable variations in a set of gravity-sensitive features in its near-IR spectrum (Allers & Liu 2013). These features include the FeH bands at 0.99, 1.20, and 1.55 μm; Na I lines at 1.14 and 2.21 μm; K I lines at 1.17 and 1.25 μm; the VO band at 1.06 μm; and the shape of the *H*-band continuum. Allers & Liu (2013), through the examination of spectra from 73 ultracool dwarfs, established a gravity score for four indicators: FeH, VO, alkali lines, and H-band continuum shape. They assigned a score of 0 to objects following the field gravity (FLD-G), a score of 1 to moderate-gravity (INT-G or β)

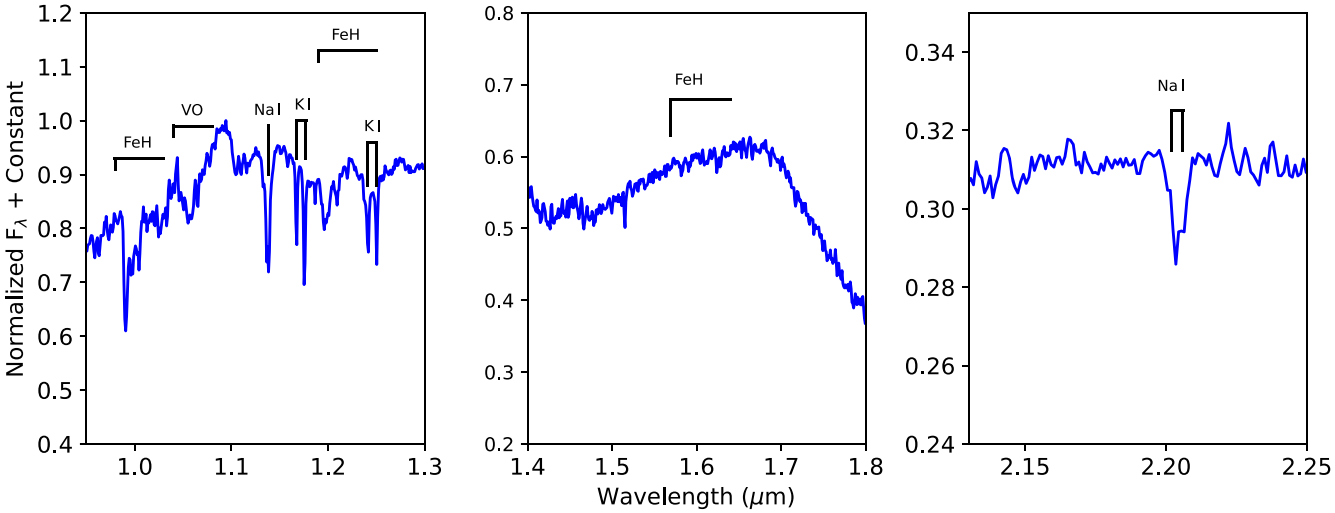

Figure 4. Gravity-sensitive spectral features in in the NIRISS spectrum.

objects, and a score of 2 to low-gravity objects (Allers & Liu 2013).

TRAPPIST-1 is most likely a field-age star (e.g., Gizis et al. 2000; Filippazzo et al. 2015; Gonzales et al. 2019). However, the weaker FeH absorption lines and a triangular shape in the *H* band, observed in its spectrum, indicate characteristics associated with low surface gravity objects typically found in young stellar associations (e.g., Allers & Liu 2013; Gillon et al. 2016; Burgasser & Mamajek 2017).

A closer examination of the kinematic analysis by Burgasser & Mamajek (2017) contradicts this notion, suggesting that TRAPPIST-1 is relatively old. They estimated the age of TRAPPIST to be approximately 7.6 ± 2.2 billion years, considering various factors, such as kinematics, stellar density, spectral indices, rotation, activity, and metallicity. This conclusion is supported by the absence of enhanced VO absorption in the SpeX prism spectrum (Burgasser & Mamajek 2017). They classified TRAPPIST-1 as an intermediate-gravity object (INT-G; Burgasser & Mamajek 2017).

Gonzales et al. (2019) conducted a comprehensive analysis of TRAPPIST-1, measuring the Allers & Liu (2013) indices and comparing them with a broader sample, employing spectra obtained from SpeX and FIRE instruments. In this study, we investigate the behavior of these indices using the same approach but employing the NIRISS spectrum instead (see Figure 4) and juxtapose our findings with theirs. We computed the gravity-sensitive spectral indices using Equation (1) of Allers & Liu (2013). Detailed values of these indices, along with the resulting gravity scores and measurements from Gonzales et al. (2019), are provided in Table 2.

TRAPPIST-1 scored 1 across all gravity indices in the NIRISS spectrum (refer to Table 9 of Allers & Liu 2013), indicating an intermediate-gravity (INT-G) level. Our study's gravity scores align with those obtained from the SpeX low-resolution data. Additionally, all measurements of the FeH_z index using NIRISS, SpeX, and FIRE spectra fall within the intermediate-gravity range. However, the FIRE (low- and medium-resolution spectra) data and SXD (only in medium-resolution spectra) data yielded a score of 0 for the H-cont and KI_J indices, respectively, suggesting field gravity. Nevertheless, at this stage, following Gonzales et al. (2019), we suggest an intermediate-gravity level for TRAPPIST-1.

Furthermore, we measured the EWs of gravity-sensitive alkali lines using NIRISS data. Derived values of the EWs, along with measurements from Gonzales et al. (2019), are provided in Table 3. The method for calculating EWs is described in Section 3.1.

In the NIRISS spectrum, all gravity-sensitive lines received a score of 0 except for K I at 1.169 and 1.253 μm (refer to Table 10 of Allers & Liu 2013). Similarly, in the FIRE spectrum, the K I lines at 1.169 and 1.253 μm were scored as 1, while the K I line at 1.177 μm obtained a score of 0. However, in the SXD spectrum, all three K I lines received a score of 0 (Gonzales et al. 2019).

Through band-by-band comparisons among the NIRISS, FIRE, and SpeX data, TRAPPIST-1 displays a blend of both field and young spectral features. Our findings support the conclusions drawn by Gonzales et al. (2019). They conducted further analysis, such as examining spectral indices versus spectral type in their sample, and found that TRAPPIST-1 lies in the β gravity class, though when considering EW versus spectral type, TRAPPIST-1 aligns more closely with a field source (Gonzales et al. 2019).

To reconcile these discrepancies, Gonzales et al. (2019) proposed that TRAPPIST-1 is likely a field-age star with spectral features reminiscent of low surface gravity objects. They suggested two potential causes for these indicators: tidal interactions with its planets and magnetic activity. Observations of rotational variability (Luger et al. 2017; Vida et al. 2017) provide indications of magnetic activity.

According to the findings of Gonzales et al. (2019), TRAPPIST-1 is not a spectral oddity. They identified several other stars with similar spectral peculiarities, including the M8 dwarf LHS 132 and the M9β dwarf 2MASS J10220489 +0200477, as well as the L1β 2MASS J10224821+5825453 and the L0β 2MASS J23224684–3133231. These stars exhibit distinct kinematics, making them all intriguing candidates for future exoplanet studies (Gonzales et al. 2019).

3.3. Chromospheric Feature Identifications and Activity Indicators

Many M dwarfs exhibit active chromospheres and produce strong flares that outshine solar flares in terms of energy released (Gray & Corbally 2009). This is evident from the detectable

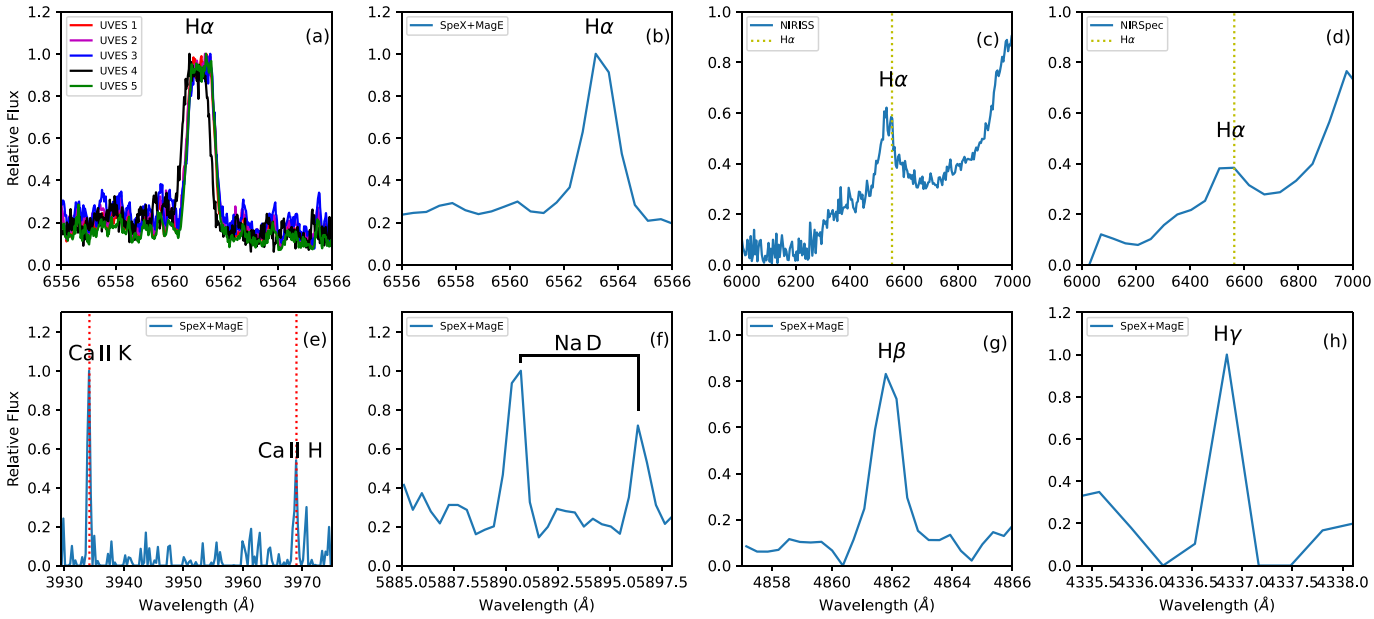

Figure 5. Activity indicators of TRAPPIST-1 in the SpeX+MagE and UVES spectra.

Table 2
Allers & Liu Gravity Indices of TRAPPIST-1 Measures Using the NIRISS, SpeX, and FIRE Data

Spectrum	References	FeH_z Index	VO_z Index	KI_J Index	H-cont Index	Gravity Scores[a]	Gravity Class
NIRISS	This study	1.089 ± 0.011	1.068 ± 0.009	1.064 ± 0.010	0.972 ± 0.013	1n11	INT-G
SpeX-SXD (M)	Gonzales et al. (2019)	1.119 ± 0.001	1.070 ± 0.002	1.070 ± 0.001	0.971 ± 0.001	1n01	INT-G
FIRE (M)	Gonzales et al. (2019)	1.105 ± 0.001	1.084 ± 0.001	1.062 ± 0.001	0.951 ± 0.001	1n10	INT-G
SpeX prism (L)	Gonzales et al. (2019)	1.078 ± 0.008	1.054 ± 0.003	1.059 ± 0.010	0.981 ± 0.008	1n11	INT-G
SpeX-SXD (L)	Gonzales et al. (2019)	1.119 ± 0.001	1.070 ± 0.002	1.070 ± 0.001	0.971 ± 0.001	1n11	INT-G
FIRE (L)	Gonzales et al. (2019)	1.105 ± 0.001	1.084 ± 0.001	1.062 ± 0.001	0.951 ± 0.001	1n10	INT-G

Note. In the first column, M and L refer to medium and low resolutions, respectively.
[a] Gravity scores are as follows: 0—field gravity (FLD-G); 1—intermediate gravity (INT-G). For M8 dwarfs, the VO_z value has no index score and thus is labeled as "*n*" following Gonzales et al. (2019).

Table 3
Equivalent Widths Calculated from Medium-resolution Spectra for TRAPPIST-1

Spectrum	References	Na I (1.138 μm) EW (Å)	K I (1.169 μm) EW (Å)	K I (1.177 μm) EW (Å)	K I (1.253 μm) EW (Å)
NIRISS	This study	11.81 ± 0.17	3.78 ± 0.23	6.43 ± 0.19	4.05 ± 0.24
SpeX-SXD	Gonzales et al. (2019)	11.762 ± 0.095	4.566 ± 0.084	6.891 ± 0.073	4.618 ± 0.067
FIRE	Gonzales et al. (2019)	12.049 ± 0.015	3.913 ± 0.019	6.690 ± 0.014	4.027 ± 0.014

emissions observed in hydrogen lines (Hα at 6562.8 Å, Hβ at 4861.3 Å, Hγ at 4337.5 Å), as well as the Ca II lines (Ca II H and K at 3969 and 3934 Å) and the Na I D at 5891.58 and 5897.56 Å, which are indicators of stellar activity (Long et al. 2018; Schöfer et al. 2019; Su et al. 2022). This section outlines a more comprehensive list of chromospheric activity indicators of TRAPPIST-1 and their corresponding measurements.

We identified the Hα emission in the UVES, SpeX+MagE, NIRISS, and NIRSpec spectra (Figures 5(a), (b), (c), and (d)) and conducted an analysis of these lines in Section 3.3.1. Additionally, Ca II lines were detected in the SpeX+MagE spectrum in Figure 5(e). The Na I D and hydrogen lines also were observed in the SpeX+MagE spectra, as depicted in Figures 5(f), (g), and (h). The characteristics of these lines, including their line center, EW, and emission flux, are provided in Table 4. The methodology for determining EWs is elaborated on in Section 3.1. Furthermore, we measured the emission-line fluxes by integrating the flux over the line profile in the SpeX+MagE spectrum.

3.3.1. Hα Emission

Balmer-alpha at 656.2 ± 3.05 nm is the primary indicator of magnetic heating and activity in low-mass stars, which traces the presence of gas at temperatures of 5000–10,000 K (Lee et al. 2010). TRAPPIST-1, like other ultracool stars, displays a

Table 4
Line Measurements for Some Emission Lines of TRAPPIST-1 Using the SpeX +MagE Spectrum

Line	λ (Å)	EW (Å)	Emission Line Flux (10^{-18} erg cm^{-2} s^{-1} Å^{-1})
Hβ	4861.73	-3.42 ± 0.21	123 ± 40
Hγ	4336.82	-3.26 ± 0.18	103 ± 46
Na I D	5890.68	-3.86 ± 0.19	67 ± 37
Na I D	5896.39	-2.18 ± 0.22	88 ± 48
Ca II K	3933.99	-4.68 ± 0.20	127 ± 64
Ca II H	3968.82	-2.94 ± 0.19	265 ± 43

notable Hα line. Although, in late M dwarfs, Hα emission is not a reliable indicator of youth (Kirkpatrick et al. 2008), TRAPPIST-1 produces numerous strong flares and has persistent chromospheric activity, as indicated by its fraction of luminosity related in Hα emission, $L_{\mathrm{H}\alpha}/L_{\mathrm{bol}} = (2.5\text{–}4.0) \times 10^{-5}$, with an H$\alpha$ EW of 4.9 Å (Vida et al. 2017; Paudel et al. 2019). This ratio gauges the strength of the active emission in relation to the star's overall energy budget, making it an accurate indicator of activity regardless of the continuous flux within a specific wavelength range (Reid & Hawley 2005).

In this study, we conducted measurements of the Hα emission line using our collected data, as presented in Table 5, across UVES and SpeX+MagE spectra. The relative Hα luminosity was computed through $L_{\mathrm{H}\alpha}/L_{\mathrm{bol}} = \chi(\mathrm{H}\alpha) \times \mathrm{EW}(\mathrm{H}\alpha)$, where $\chi(\mathrm{H}\alpha)$ is the ratio of continuum flux around Hα to the bolometric flux (West & Hawley 2008). We also incorporated the measurements from Burgasser et al. (2015) and Gizis et al. (2000) into Table 5. Our measurement aligns with previous studies and establishes a range for the Hα strength, with lower and upper bounds set at [−4.73, −4.57]. Compared to other late M dwarfs, specifically M8.0 ± 1.0 spectral class studied in West et al. (2004), TRAPPIST-1 displays moderate Hα activity.

It is worth noting that we did not use the NIRISS and NIRSpec spectra for Hα measurements. While Hα emission is detectable in these spectra (Figures 5(c) and (d)), the observed Hα line is notably broader compared to the UVES and SpeX+MagE spectra, rendering them inadequate for precise measurements.

4. Photospheric Modeling of TRAPPIST-1 with JWST Data

4.1. Model Description

Low-to-moderate-resolution spectra from JWST, such as those attainable with NIRSpec/PRISM and NIRISS/SOSS, are expected to prominently highlight the effects of stellar contamination on transit transmission spectroscopy and the precision of related inferences due to their rich information content (see, e.g., Rackham et al. 2023). In this context, the temptation to assess photosphere modeling with JWST data arises. Following previous analyses of the space-based spectra of TRAPPIST-1 (Zhang et al. 2018; Wakeford et al. 2019; Garcia et al. 2022; Lim et al. 2023), we modeled TRAPPIST-1's median out-of-transit NIRISS and NIRSpec spectra while considering the possible contributions of surface heterogeneities like spots and faculae. We assume, as in other studies (e.g., Rackham et al. 2017; Garcia et al. 2022; Narrett et al. 2024), that the entire photosphere may be represented as a mixture of regions with varying temperatures, allowing us to present the star's spectrum as follows:

Table 5
Hα Measurement of TRAPPIST-1 Using the SpeX+MagE and UVES Spectra

Spectrum	References	EW(Hα) (Å)	$\lambda_{\mathrm{H}\alpha}$ (Å)	$\log(L_{\mathrm{H}\alpha}/L_{\mathrm{bol}})$
UVES 1	This study	-4.26 ± 0.31	6560.96	-4.57 ± 0.08
UVES 2	This study	-3.84 ± 0.26	6561.19	-4.63 ± 0.06
UVES 3	This study	-4.09 ± 0.21	6561.12	-4.61 ± 0.05
UVES 4	This study	-3.68 ± 0.25	6561.15	-4.66 ± 0.07
UVES 5	This study	-3.39 ± 0.22	6561.14	-4.70 ± 0.05
SpeX +MagE	Burgasser et al. (2015)	-4.86 ± 0.18	6563.21	-4.73 ± 0.06
Ritchey–Chretien	Gizis et al. (2000)	4.9	⋯	−4.61

$$F = (1 - f_2 - f_3)F_1 + f_2 F_2 + f_3 F_3. \quad (2)$$

The covering fractions, denoted as f_2 and f_3, represent the fractional contributions of secondary and tertiary spectral components, such as spots and faculae, to the integrated spectrum. F_1, F_2, and F_3 stand for the intrinsic spectra of the primary, secondary, and tertiary components, respectively. While our fitting procedure is agnostic to the physical origin of these spectra, this model is motivated by the expectation that the quiescent photosphere, spots, and faculae each distinctly contribute to the integrated spectrum. The component spectra were treated as representative of photospheric components in all positions, and limb-darkening effects were not taken into account, following previous analyses (Rackham et al. 2018; Rackham et al. 2019; Rackham & de Wit 2023; Wakeford et al. 2019; Garcia et al. 2022; Lim et al. 2023; Narrett et al. 2024). This straightforward model operates on the premise that surface heterogeneities possess spectra akin to a global photosphere but at varying temperatures. We emphasize that f_2 and f_3 can be zero, simplifying the model to one or two temperature components.

Three heterogeneity models are derived from Equation (2), each with one, two, and three temperature components, respectively. The "1-comp" model depicts a quiescent star where only the spectrum of the quiescent photosphere appears across the stellar surface. Following this, the "2-comp" model represents a star with two spectral components, e.g., the quiescent photosphere and spots. The "3-comp" model portrays a star with three spectral components, e.g., the quiescent photosphere, spots, and faculae.

To generate the model spectra associated with stellar surface heterogeneities, we employed the PHOENIX ACES[11] (Husser et al. 2013) and SPHINX (Iyer et al. 2022, 2023) stellar atmosphere models. The parameter space covered by both grids aligns with our requirements: the PHOENIX grid encompasses surface gravities ranging from 0.0 to 6.0 in 0.5 increments and effective temperatures ranging from 2300 to 7000 K with 100 K intervals. The SPHINX grid covers surface gravities ranging from 4.0 to 5.5 with intervals of 0.25 and effective temperatures ranging from 2000 to 4000 K with intervals of 100 K. We utilized models with [Fe/H] = 0 from both grids, as this is the closest metallicity to TRAPPIST-1 ([Fe/H] = 0.052 ± 0.073; this study).

[11] https://phoenix.astro.physik.uni-goettingen.de/

Table 6
Free Parameters and Their Priors for the Three Heterogeneity Models

Model	T (K)	f_1	f_2	f_3	$R_\star$ ($R_\odot$)	Distance (pc)	Scaling Factor	$\ln f_{\rm var}$
1-comp	$\mathcal{U}(2300, 5500)$ $\mathcal{U}(2000, 4000)$	$D(0, 1)$	⋯	⋯	$\mathcal{N}(0.1192, 0.0013)$	$\mathcal{N}(12.467, 0.011)$	$\mathcal{U}(0, 10)$	$\mathcal{U}(-50, 0)$
2-comp	$\mathcal{U}(2300, 5500)$ $\mathcal{U}(2000, 4000)$	$D(0, 1)$	$D(0, 1)$	⋯	$\mathcal{N}(0.1192, 0.0013)$	$\mathcal{N}(12.467, 0.011)$	$\mathcal{U}(0, 10)$	$\mathcal{U}(-50, 0)$
3-comp	$\mathcal{U}(2300, 5500)$ $\mathcal{U}(2000, 4000)$	$D(0, 1)$	$D(0, 1)$	$D(0, 1)$	$\mathcal{N}(0.1192, 0.0013)$	$\mathcal{N}(12.467, 0.011)$	$\mathcal{U}(0, 10)$	$\mathcal{U}(-50, 0)$

Note. $\mathcal{U}(2300, 5500)$ and $\mathcal{U}(2000, 4000)$ in the second column belong to PHOENIX and SPHINX grids, respectively. $D(0, 1)$ represents a Dirichlet distribution with parameters (0, 1).

We performed linear interpolation across $T_{\rm eff}$ and $\log g$ grid points using the `Speclib` Python package[12] (Rackham 2023). We placed a uniform prior on the temperatures of the spectral components, covering temperatures from 2300 to 5500 K for the PHOENIX grid and from 2000 to 4000 K for the SPHINX grid, with $\log g$ values between 5.0 and 5.5, to obtain spectra with a surface gravity close to $\log g = 5.2396^{+0.0056}_{-0.0073}$ cm s^{-2} (Agol et al. 2021). The process was efficiently executed using the `SpectralGrid` object in Speclib, involving loading a spectral grid into memory once with fixed metallicity and surface gravity values and then employing linear interpolation between temperature grid points to generate the sample spectra (Rackham 2023). Finally, the spectra were convolved with a Gaussian profile and resampled to match the resolution and pixel sampling of the associated NIRISS and NIRSpec data.

4.2. Sampling Procedure

We fitted the out-of-transit spectra of NIRISS and NIRSpec to these three models, each exploring various covering fractions representing the host star's photospheric heterogeneity. This fitting process involves the nested sampling algorithm using the `UltraNest` Python package (Buchner 2021) to derive the posterior probability distributions of the model parameters. At each sampling step, we leveraged the Speclib package to generate the component spectra incorporated in the model. Slice sampling was used to effectively explore the parameter space, setting the number of steps at 10 times the number of parameters.

We placed uniform priors on temperature in the model fluxes and for the covering fractions, as well as normal priors for the distance and radius of the star (refer to Table 6). The unit of flux density at the stellar surface for these models is erg s^{-1} cm^{-2} Å^{-1}, which we convert to flux density at Earth, considering TRAPPIST-1's angular diameter $\left(\left(\frac{R_\star}{d}\right)^2\right)$, calculated using its stellar radius $R_\star = 0.1192 \pm 0.0013\ R_\odot$ (Agol et al. 2021) and distance 12.467 ± 0.011 pc (Gaia Collaboration et al. 2023). We placed a Dirichlet prior[13] on the coverage fractions to ensure that they sum to 1.

To account for uncertainties on the JWST flux calibration and other aspects of the data reduction that may lead to offsets in flux, we included a scaling parameter as a free parameter with a uniform prior over a wide range from 0.1 to 10. We also fit for the natural logarithm of an extra noise term that encapsulates any additional noise present in the data ($\ln f_{\rm var}$), the amplitude of which scales with the model flux, following Rackham & de Wit (2023) and Foreman-Mackey et al. (2013, 2019). For the natural logarithm of the likelihood function, we adopted Equation (2) of Rackham & de Wit (2023), which identifies the values that maximize the likelihood of the models when compared to the observed data.

4.3. Results

Figure 6 displays results using the PHOENIX grid, while Figure 7 presents results applying the SPHINX grid. Table 7 displays the posterior model parameters and their associated uncertainties, along with the reduced χ^2, the Akaike information criterion (AIC; Akaike 1998) values, and Akaike weights serving as indicators of the statistical goodness of fit and the complexity of the model for 12 fits. Fits 1–6 are derived using the PHOENIX grid, while fits 7–12 are obtained using the SPHINX grid.

The first finding relates to the model dependence of the inferred stellar properties. Indeed, while the effective temperature of the dominant surface feature (T_1), for example, is consistent within the inferred uncertainties for a set of retrievals with a given stellar model, it significantly differs between models. For example, a fit of the NIRISS data with 1-comp using PHOENIX (fit 1) yields $T_1 = 2662^{+4}_{-4}$ K, while using SPHINX (fit 7) yields $T_1 = 2567^{+5}_{-5}$ K. In other words, while the instrument can yield constraints on the effective temperature T_1 to within ∼4 K, differences between stellar models (or their lack of fidelity) give rise to discrepancies between fits at the level of ∼100 K. Such a model-driven accuracy wall in the JWST era has previously been reported for opacity models (Niraula et al. 2022, 2023).

Overall, similar to the findings in Wakeford et al. (2019) and Garcia et al. (2022), the χ^2_r values for all fits indicate that none of them sufficiently align with the observed data. On closer examination, it is evident that the fits derived from the SPHINX grid (fits 7–12) provide a more accurate depiction of the data, as evidenced by their lower χ^2_r and AIC values compared to the fits obtained from the PHOENIX grid (fits 1–6). For 2-comp and 3-comp models, at wavelengths higher than 3 μm, fits derived from the PHOENIX grid align better with the NIRSpec data than fits derived from the SPHINX grid. However, between 2.1 and 2.4 μm, the 1-comp fits derived from the SPHINX grid align very well with the NIRISS data. Around the 1 μm region and the peak of the "triangular" shape in the H-band region, the most pronounced discrepancies are observed

[12] https://github.com/brackham/speclib
[13] See https://johannesbuchner.github.io/UltraNest/priors.html.

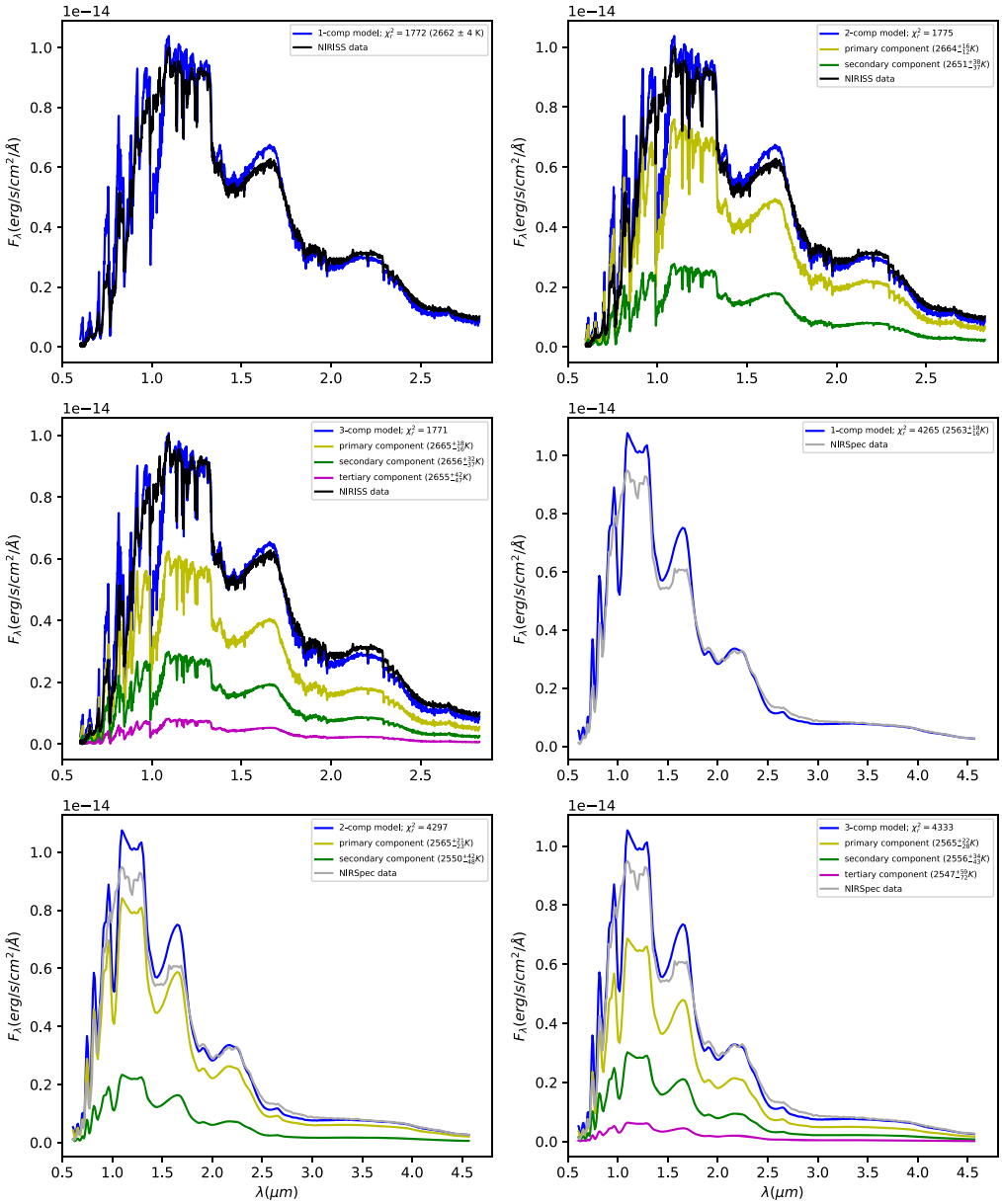

Figure 6. Photospheric modeling of TRAPPIST-1 using the NIRISS and NIRSpec out-of-transit stellar spectra. The modeling was conducted based on the PHOENIX spectral grid.

between the fits derived from the SPHINX and PHOENIX grids and the observed data.

In all tests conducted (12 fits), whether utilizing SPHINX or PHOENIX grids and whether accompanied by NIRISS or NIRSPEC observed data, the χ^2_r and the AIC indicators consistently demonstrate lower values for the 1-com fits compared to the 2-comp and 3-comp fits. Consequently, in this regard, the inferences drawn from fits derived from both the SPHINX and PHOENIX grids are aligned. This result is somewhat surprising given that TRAPPIST-1's photosphere is known to be heterogeneous, as shown by its photometric variability (e.g., Luger et al. 2017; Morris et al. 2018) and the contaminated and variable transmission spectra observed in the system (Zhang et al. 2018; Wakeford et al. 2019; Garcia et al. 2022; Lim et al. 2023). Moreover, the high values of $\ln f_{\rm var}$ retrieved in the fits (≈ -1.6; see the Appendix) show that the data uncertainties need to be inflated to $\approx e^{-1.6} = 0.20$ of the total flux level to reach an adequate fit with respect to the models. We interpret this as a clear indication that currently available models lack the fidelity necessary to effectively distinguish the spectral components present in heterogeneous photospheres, particularly for M dwarfs (see Rackham & de Wit 2023).

When assessing the AIC weights, which indicate the extent of predictive power contributed by the model under evaluation relative to the entire pool of models (Wagenmakers & Farrell 2004), discrepancies in Akaike weights across the four retrieval sets (1–3, 4–6, 7–9, 10–12) reveal a preference for the 1-comp fit (approximately 95% weight). However, the 2-comp fit (around 5% weight) generally fails to propose an alternative solution, often assigning similar temperatures to additional components without adequately restricting the covering fractions. Notably, one fit diverging from this overarching pattern is fit 8 (utilizing the SPHINX grid and the NIRISS spectrum),

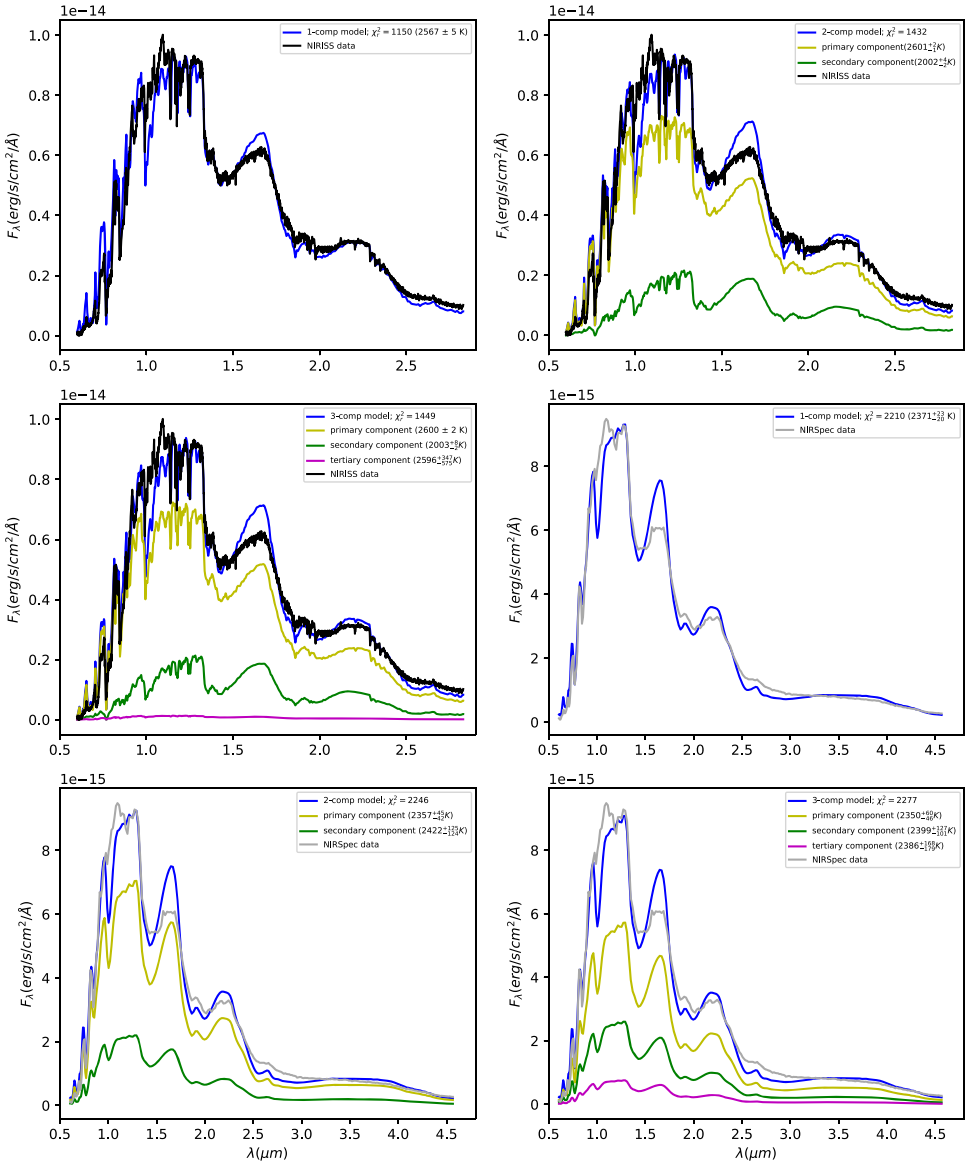

Figure 7. Photospheric modeling of TRAPPIST-1 using the NIRISS and NIRSpec out-of-transit stellar spectra. The modeling was conducted based on the SPHINX spectral grid.

where the distinctions between T_1 and T_2 are notable solely within this fit. Despite receiving approximately 5% weight overall within its fit set, akin to other 2-comp fits, it stands out by delineating a photosphere with two roughly equal yet distinctly separate components. This fit contrasts starkly with other 2-comp fits (2, 5, and 11), especially fit 2, which employs the same data set but relies on PHOENIX models. The likely explanation for this disparity lies in the temperature constraints of the PHOENIX models compared to the SPHINX models, particularly evident when models interpolate for $T \ll 2500$ K, describing the temperature of the secondary component.

In addition, as a test, we conducted another set of model fits allowing $\log g$ to vary as a free parameter, which resulted in a better fit for the PHOENIX models. However, this approach often leads to unphysical values of the star's surface gravity. This underscores the current limitations of M dwarf atmosphere models. In any case, the generally poor quality of the model fits, relative to the data precision, highlights the pressing need for improvement in M dwarf atmosphere models.

5. Spectral Energy Distribution of TRAPPIST-1

M-type dwarfs emit the majority of their energy in the IR region of the electromagnetic spectrum (Reid & Hawley 2000). However, due to Earth's atmosphere blocking IR radiation, only a fraction of their SED is observable from the ground. To overcome this limitation, we employed the NIRSpec and NIRISS spectra alongside atmosphere models to extract the SED of this ultracool M dwarf in the wavelength range of 0.6–5 μm (Figure 8).

To underscore the importance of model fidelity, as discussed in Section 4, we conducted SED analyses using both SPHINX and PHOENIX atmospheric grids. This approach enables us to illustrate how model uncertainties affect the SED analysis. We employed models with [Fe/H] = 0 and $\log_{10}(g) = 5.25$ from the SPHINX grid and models with [Fe/H] = 0 and $\log_{10}(g) = 5.0$ and 5.5 from the PHOENIX grid, as these are the closest metallicity and surface gravity to TRAPPIST-1 ($\log_{10}(g) = 5.2396^{+0.0056}_{-0.0073}$ cm s^{-2}, Agol et al. 2021; [Fe/H] = 0.052 ± 0.073, this study). Then, we performed linear

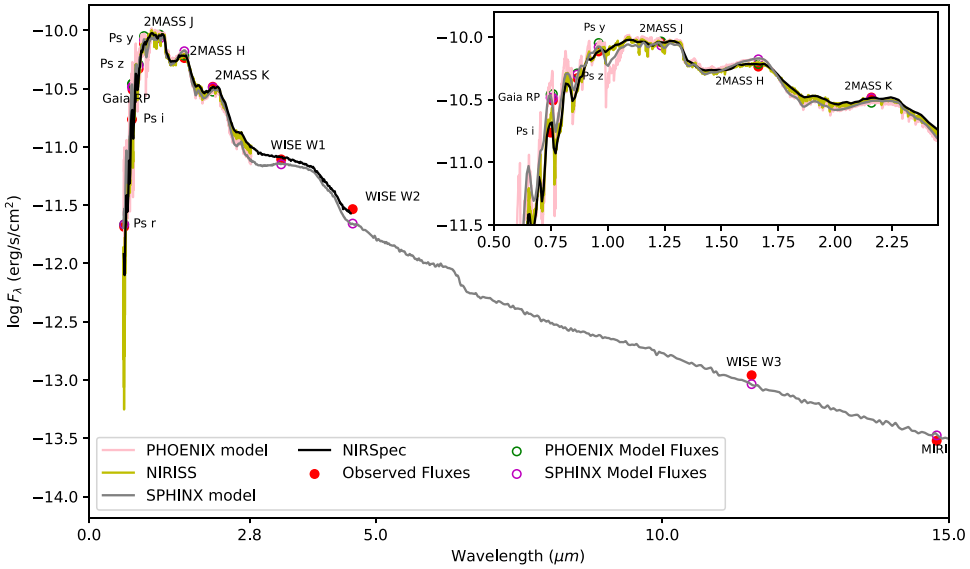

Figure 8. Near-IR and IR SED of TRAPPIST-1. Red symbols represent the observed photometric measurements. Blue symbols are the model fluxes from the best-fit SPHNIX atmosphere model (gray). Overlaid on the model are the absolute flux-calibrated spectrophotometric observations from NIRISS (yellow) and NIRSpec (black).

Table 7
Multiple-temperature Model Parameters Inferred from the NIRISS and NIRSpec Out-of-transit Spectra by PHOENIX and SPHINX Grids

Fit	T (K)	f_1	f_2	f_3	χ_r^2	AIC	Akaike Weight
1	$T_1 = 2662^{+4}_{-4}$	…	…	…	1772	−12.76	0.9465
2	$T_1 = 2664^{+16}_{-12}$, $T_2 = 2651^{+38}_{-37}$	$0.73^{+0.21}_{-0.16}$	$0.27^{+0.21}_{-0.16}$	…	1775	−6.76	0.0471
3	$T_1 = 2665^{+18}_{-16}$, $T_2 = 2656^{+32}_{-37}$, $T_3 = 2655^{+42}_{-47}$	$0.60^{+0.19}_{-0.12}$	$0.29^{+0.11}_{-0.13}$	$0.08^{+0.10}_{-0.07}$	1771	−2.76	0.0064
4	$T_1 = 2563^{+18}_{-16}$	…	…	…	4265	−8.55	0.9464
5	$T_1 = 2565^{+21}_{-23}$, $T_2 = 2550^{+42}_{-48}$	$0.78^{+0.18}_{-0.19}$	$0.22^{+0.19}_{-0.18}$	…	4297	−2.55	0.0472
6	$T_1 = 2565^{+22}_{-28}$, $T_2 = 2556^{+34}_{-43}$, $T_3 = 2547^{+59}_{-72}$	$0.63^{+0.20}_{-0.14}$	$0.28^{+0.11}_{-0.15}$	$0.06^{+0.11}_{-0.05}$	4333	1.45	0.0064
7	$T_1 = 2567^{+5}_{-5}$	…	…	…	1150	−12.77	0.9464
8	$T_1 = 2601^{+2}_{-1}$, $T_2 = 2002^{+4}_{-2}$	$0.55^{+0.02}_{-0.02}$	$0.45^{+0.02}_{-0.02}$	…	1432	−6.77	0.0472
9	$T_1 = 2600^{+2}_{-2}$, $T_2 = 2003^{+8}_{-2}$, $T_3 = 2596^{+347}_{-575}$	$0.54^{+0.03}_{-0.03}$	$0.44^{+0.03}_{-0.06}$	$0.01^{+0.07}_{-0.01}$	1449	−2.77	0.0064
10	$T_1 = 2371^{+23}_{-20}$	…	…	…	2210	−8.55	0.9465
11	$T_1 = 2357^{+45}_{-42}$, $T_2 = 2422^{+125}_{-124}$	$0.78^{+0.14}_{-0.18}$	$0.22^{+0.18}_{-0.14}$	…	2246	−2.55	0.0471
12	$T_1 = 2350^{+60}_{-46}$, $T_2 = 2399^{+127}_{-101}$, $T_3 = 2386^{+168}_{-179}$	$0.64^{+0.17}_{-0.14}$	$0.27^{+0.11}_{-0.12}$	$0.08^{+0.10}_{-0.06}$	2277	1.45	0.0064

Note. The fits in the first column encompass a total of 12 configurations, categorized as follows: (1) 1-comp (using PHOENIX and NIRISS), (2) 2-comp (using PHOENIX and NIRISS), (3) 3-comp (using PHOENIX and NIRISS), (4) 1-comp (using PHOENIX and NIRSpec), (5) 2-comp (using PHOENIX and NIRSpec), (6) 3-comp (using PHOENIX and NIRSpec), (7) 1-comp (using SPHINX and NIRISS), (8) 2-comp (using SPHINX and NIRISS), (9) 3-comp (using SPHINX and NIRISS), (10) 1-comp (using SPHINX and NIRSpec), (11) 2-comp (using SPHINX and NIRSpec), (12) 3-comp (using SPHINX and NIRSpec).

interpolation across $T_{\rm eff}$ grid points using the `Speclib` package (Rackham 2023), as discussed earlier in Section 4. Subsequently, we fitted the out-of-transit spectra of NIRISS and NIRSpec to these models to derive the appropriate models for this M dwarf.

We used the broadband photometry-based fluxes as the observed SED. This encompassed J, H, and K_S magnitudes from 2MASS (Cutri et al. 2003); W1–W3 magnitudes from the Wide-field Infrared Survey Explorer (WISE; Cutri et al. 2012); R_P magnitude from Gaia (Gaia Collaboration et al. 2016, 2018); P_sy, P_sz, P_si, and P_sr magnitudes from Pan-STARRS (Gonzales et al. 2019); and MIRI flux at 14.79 μm (Greene et al. 2023). We also plotted the NIRISS and NIRSpec data on the SED diagram.

We followed the SED fitting procedures outlined by Stassun & Torres (2016). Consistent with their assumptions, considering TRAPPIST-1's close distance of 12.467 ± 0.011 pc (Gaia Collaboration et al. 2023), we assumed zero extinction (A_V). We calculated the predicted flux values from the appropriate SPHINX and PHOENIX models at the same wavelengths as our photometric measurements to generate the best-predicted model SED. An overall normalization factor was then applied to shift the entire model up or down in flux to align with the observed fluxes. To obtain the best-fit SED model, we fitted the atmosphere model to the observed photometric fluxes to minimize χ_r^2 by varying just two fit parameters: effective temperature and overall normalization. We iterated over various choices for the overall normalization factor and calculated a new χ_r^2 value each time. We selected the best SED model with the minimum χ_r^2 value corresponding to that model.

Table 8
Results of SED Analysis Using the SPHINX and PHOENIX Grids

Models	$F_{\rm bol}$ ($\times 10^{-10}$ erg s^{-1} cm^{-2})	$L_{\rm bol}$ ($L_\odot$)	$T_{\rm eff}$ (K)
SPHINX	1.1523 ± 0.0697	0.000559 ± 0.000034	2571 ± 41
PHOENIX	1.1471 ± 0.0593	0.000571 ± 0.000028	2568 ± 36
Weighted mean	1.1493 ± 0.0452	0.000566 ± 0.000022	2569 ± 28

We calculated the bolometric flux ($F_{\rm bol}$) and bolometric luminosity ($L_{\rm bol}$) by integrating the best-fit SED model across all wavelengths. Combining the bolometric flux with the stellar radius ($R_* = 0.1192 \pm 0.0013\ R_\odot$) derived from Agol et al. (2021) and the distance 12.467 ± 0.011 pc (Gaia Collaboration et al. 2023), we computed the effective temperature. All results of each model and the weighted-mean values are listed in Table 8. The relationship between these quantities is determined by

$$R_\star/d = \left(\frac{F_{\rm bol}}{\sigma_{\rm SB} T_{\rm eff}^4}\right)^{1/2}, \quad (3)$$

where d represents the distance to the star and $\sigma_{\rm SB}$ is the Stefan–Boltzmann constant (Stassun et al. 2017). The uncertainty of the effective temperature was influenced by the measurement of the SED flux and computed via the error propagation method. The SED results with both sets of models highlight how the parameters derived from such fits differ from one model to the next.

Previous studies have revealed a variety of $T_{\rm eff}$ values, including 2550 ± 55 K (Gillon et al. 2016), 2628 ± 42 K (Gonzales et al. 2019), 2520 ± 39 K (Ducrot et al. 2020), and 2566 ± 26 K (Agol et al. 2021). Gonzales et al. (2019) utilized DMEstar models to extend the hybrid cloud evolutionary models of brown dwarfs into the low-mass stellar range, such as TRAPPIST-1, and derived $T_{\rm eff} = 2628 \pm 42$ K by combining their inferred radius with the bolometric luminosity using the Stefan–Boltzmann law (Gonzales et al. 2019). The primary sources of uncertainty in their $T_{\rm eff}$ originate from the measurement of SED flux and uncertainties in the age of the system, leading to a range of possible radii. Nevertheless, Gonzales et al. (2019) acknowledged, as mentioned in Dupuy & Kraus (2013), that minor variations in radii have negligible impacts on the calculated $T_{\rm eff}$. Agol et al. (2021) also derived $T_{\rm eff} = 2566 \pm 26$ K based on the stellar luminosity and radius, but with errors estimated via Monte Carlo simulations.

This study's $L_{\rm bol}$ and $T_{\rm eff}$ values align closely with previous measurements, indicating a reassuring level of agreement across various investigations. However, it is essential to take into account the inherent uncertainties in data accuracy and measurement methodologies, which may influence slight variations in reported values.

6. Results and Discussion

In this study, we utilized NIRISS and NIRSpec spectra alongside six ground-based spectra to investigate the photospheric and chromospheric spectral characteristics of TRAPPIST-1. We measured the EWs of the Na I and Ca I absorption lines, as well as the H_2O–K2 index (Rojas-Ayala et al. 2012), and determined a metallicity for this M dwarf of $[{\rm Fe/H}] = 0.052 \pm 0.073$ dex. This finding aligns well with Gillon et al. (2017), who calculated a metallicity of 0.040 ± 0.080 dex.

We analyzed the behavior of the gravity-sensitive indices proposed by Allers & Liu (2013) in the NIRISS spectrum and juxtaposed them with measurements from the SpeX and FIRE spectra provided by Gonzales et al. (2019). Our study confirms the findings of Gonzales et al. (2019), indicating a gravity class of INT_G through gravity-sensitive indices. However, the analysis of EWs of gravity-sensitive lines suggests evidence hinting at field sources. In summary, through band-by-band comparisons of the NIRISS (this study), FIRE, and SpeX data (Gonzales et al. 2019), TRAPPIST-1 exhibits a combination of spectral features associated with both field stars and those of intermediate gravity. TRAPPIST-1 is probably a field-age star, showing spectral attributes reminiscent of youthful objects. According to the findings of Gonzales et al. (2019), TRAPPIST-1 is not a spectral oddity. They identified several other stars with similar spectral peculiarities. Anyway, this interesting result deserves a comprehensive study of TRAPPIST-1 alongside a larger sample of late-type M dwarfs.

In addition to the NIRISS spectrum, we utilized six ground-based spectra for activity indicators, including Hα emission. We established a more accurate range for the Hα strength, setting upper bounds at $[-4.73, -4.57]$. Our new measurement results are consistent with previous studies on Hα emission from TRAPPIST-1 (e.g., Gizis et al. 2000; Reiners & Basri 2010; Burgasser et al. 2015) and indicate a moderate level of stellar activity.

We utilized the NIRSpec and NIRISS spectra along with SPHINX and PHOENIX atmosphere models to derive the SED of TRAPPIST-1 across the wavelength range of 0.6–5 μm. As shown in Table 8, results using the SPHINX and PHOENIX grids differ by $\ll 1\sigma$, and we report the weighted-mean measurements here. We measured the stellar luminosity as $L_{\rm bol} = 0.000566 \pm 0.000022\ L_\odot$. Our SED-fitting-based effective temperature estimate for TRAPPIST-1 (2569 ± 28 K) is consistent with the effective temperature derived by previous studies (e.g., Gillon et al. 2016; Agol et al. 2021).

We attempted to constrain surface heterogeneities on the stellar surface of TRAPPIST-1 through photospheric modeling using JWST spectra, following similar previous studies with HST spectra (Zhang et al. 2018; Wakeford et al. 2019; Garcia et al. 2022). The comparison between fits derived from the SPHINX and PHOENIX grids reveals that the former provides a more accurate depiction of JWST data, as indicated by lower $\chi^2_{\rm red}$ and AIC values. However, similar to previous studies (Wakeford et al. 2019; Garcia et al. 2022), our analysis suggests that none of the fits sufficiently align with the observed data. Interestingly, the "1-comp" fit, derived from NIRISS data and the SPHINX grid, shows a fit comparable to those of the more complex "2–3-comp" fits, despite TRAPPIST-1's known heterogeneous photosphere. We interpret this as an indication that current models, such as PHOENIX and SPHINX, lack the exacting fidelity needed to discern such stellar heterogeneity. This could be due to both limitations in stellar models and the marginalization of unknown systematic effects with retrieval tools, leading to large data–model residuals (Rackham & de Wit 2023). In addition—as found previously for opacity models (Niraula et al. 2022, 2023), we find a model-driven accuracy wall more than one order of magnitude above the precision accessible with JWST data, due to the lack of model fidelity (e.g., intermodel differences on the derived effective temperature at the level of $\sim$100 K while the instrument-driven uncertainty is at the level of $\sim$4 K).

As highlighted by recent studies (Iyer et al. 2023, and references therein), current M dwarf atmospheric models encounter several limitations. Their reliance on traditional methods for elemental abundance derivation, effective for FGK stars, may falter owing to the intricate molecular compositions and turbulent interiors of M dwarfs. Additionally, these models exhibit notable spectral variations for the same star, possibly stemming from differences in line lists and assumptions. Inconsistencies persist when comparing parameters derived from different methods, emphasizing the necessity for improved standardization and understanding of atmospheric effects, like photospheric heterogeneity and dust physics, in M dwarfs.

Acknowledgments

We acknowledge support from the BELSPO program BRAIN-be 2.0 (Belgian Research Action through Interdisciplinary Networks) contract B2/212/P1/PORTAL. B.V.R. thanks the Heising-Simons Foundation for support. This material is based on work supported by the National Aeronautics and Space Administration under agreement No. 80NSSC21K0593 for the program "Alien Earths." The results reported herein benefited from collaborations and/or information exchange within NASA's Nexus for Exoplanet System Science (NExSS) research coordination network sponsored by NASA's Science Mission Directorate. We thank Olivia Lim for providing the NIRISS spectrum under the program JWST GO-2589 and Kevin Stevenson for his assistance. M.G. is F.R.S-FNRS Research Director.

Data Availability

Some of the data presented in this Letter were obtained from the Mikulski Archive for Space Telescopes (MAST) at the Space Telescope Science Institute. The analyzed NIRISS/SOSS observation is accessible via doi:10.17909/5f2j-f460, while the NIRSpec/PRISM observation can be accessed through doi:10.17909/ws34-yb06.

Software: JWST Science Calibration Pipeline version 1.11.4 (Bushouse et al. 2023) with calibration version 1.8.2 and data processing version 2022_4a, and CRDS version 11.16.16 with the "jwst_0421.pmap" CRDS context, SPLAT (Schneider et al. 2016; Burgasser & Splat Development Team 2017), Specutils (Astropy-Specutils Development Team 2019), PHOENIX (Husser et al. 2013), SPHINX (Iyer et al. 2023), Speclib (Rackham 2023), and the standard Python libraries numpy (Harris et al. 2020), matplotlib (Hunter 2007), astropy (Astropy Collaboration et al. 2013, 2018, 2022), numpy (Harris et al. 2020), emcee (Foreman-Mackey et al. 2013), and corner (Foreman-Mackey 2016).

Appendix
Complementary Figures

Figures 9 and 10 depict corner plots associated with nested sampling results for the fitted parameters of the 1-comp models using the PHOENIX grid, while Figures 11 and 12 illustrate results using the SPHINX grid. Each corner plot showcases marginal distributions and pairwise correlations, offering insights into parameter space exploration and nested sampling algorithm convergence.

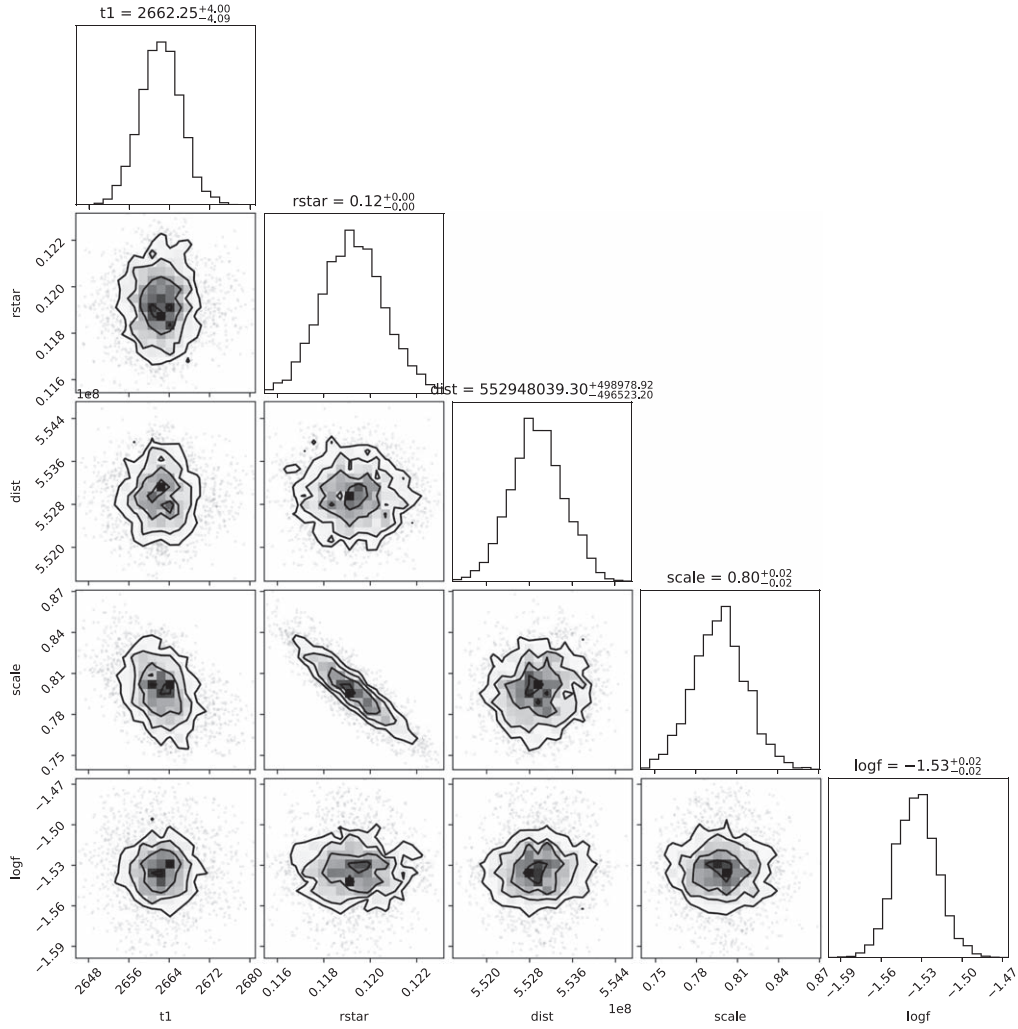

Figure 9. A corner plot of the inferred parameters of the 1-comp model. Here "t1," "rstar," "dist," "scale," and "logf" represent the temperature of the quiescent component, the star's radius, the star's distance, the scaling parameter, and additional noise present in the data, respectively. The model was constructed using the PHOENIX spectral grid and NIRISS data.

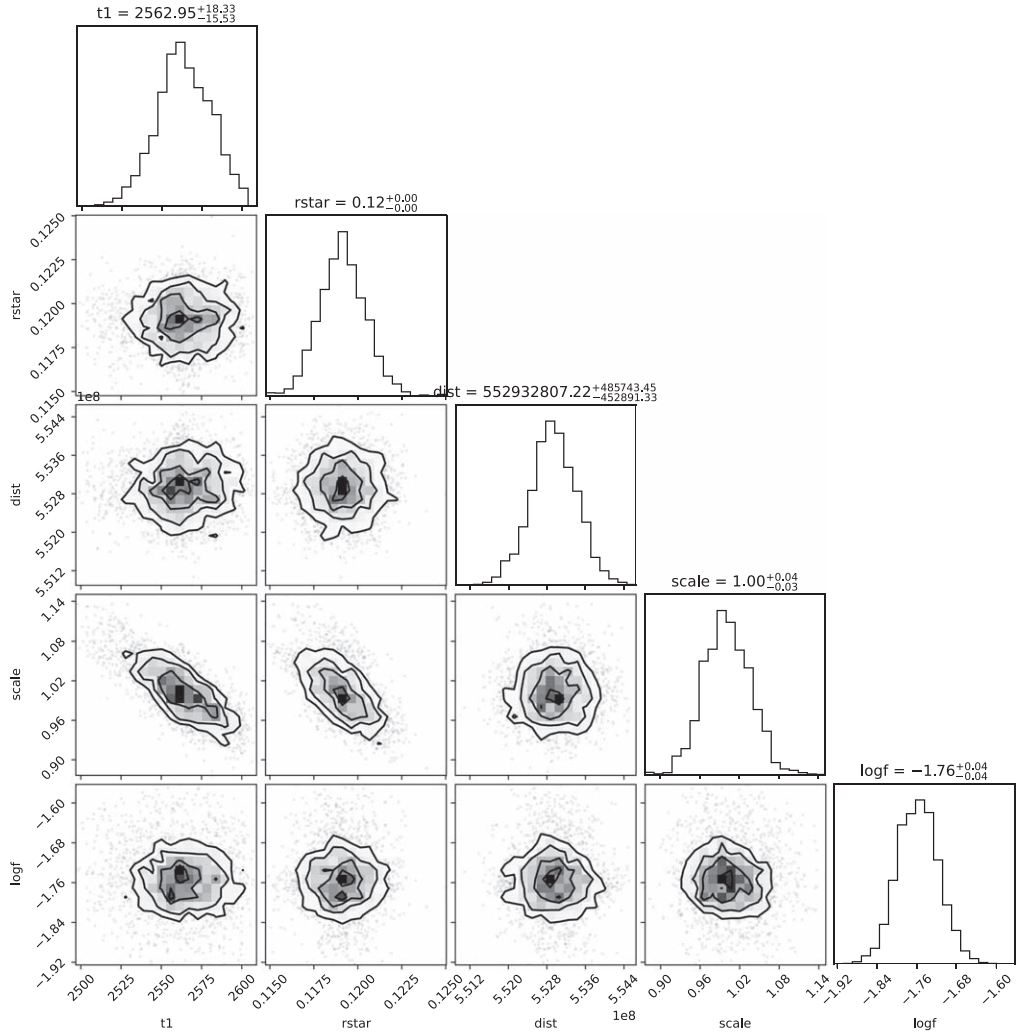

Figure 10. A corner plot of the inferred parameters of the 1-comp model. Here "t1," "rstar," "dist," "scale," and "logf" represent the temperature of the quiescent component, the star's radius, the star's distance, the scaling parameter, and additional noise present in the data, respectively. The model was constructed using the PHOENIX spectral grid and NIRSpec data.

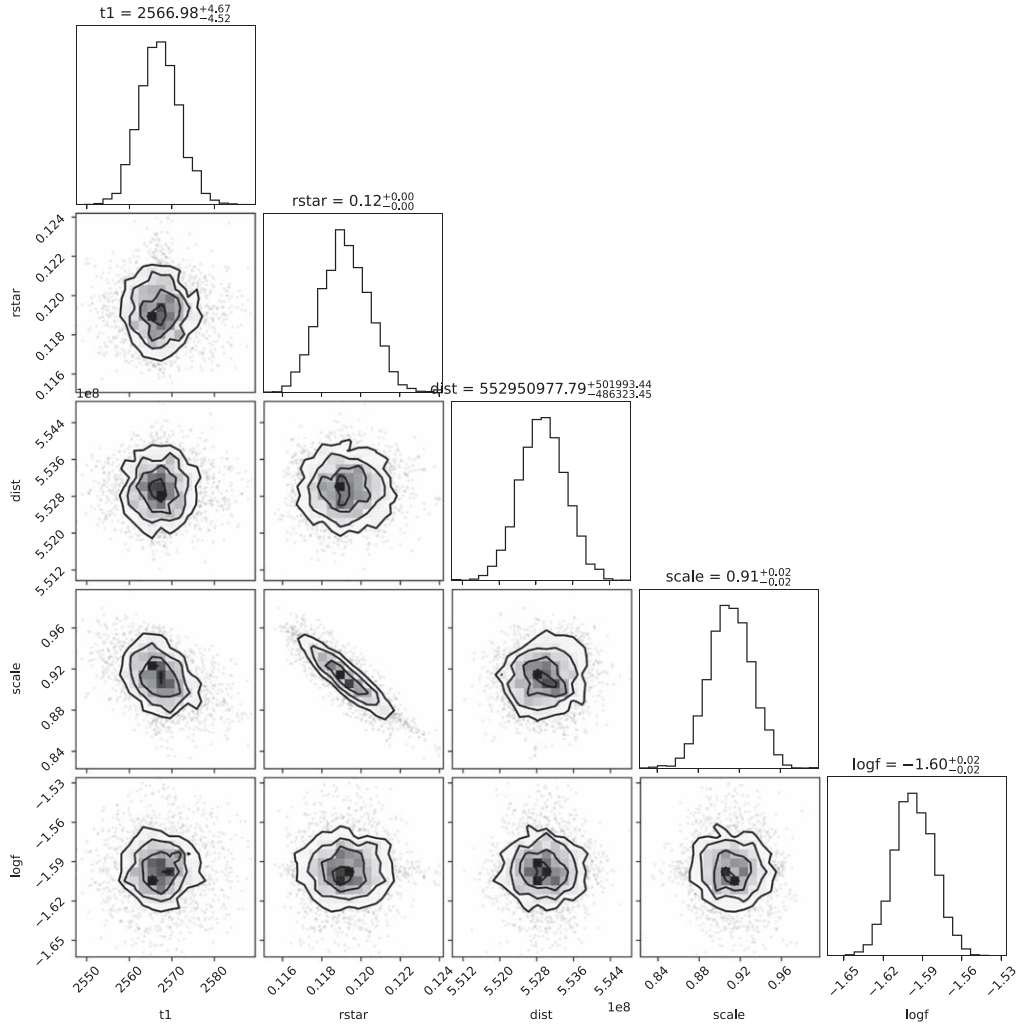

Figure 11. A corner plot of the inferred parameters of the 1-comp model. Here "t1," "rstar," "dist," "scale," and "logf" represent the temperature of the quiescent component, the star's radius, the star's distance, the scaling parameter, and additional noise present in the data, respectively. The model was constructed using the SPHINX spectral grid and NIRISS data.

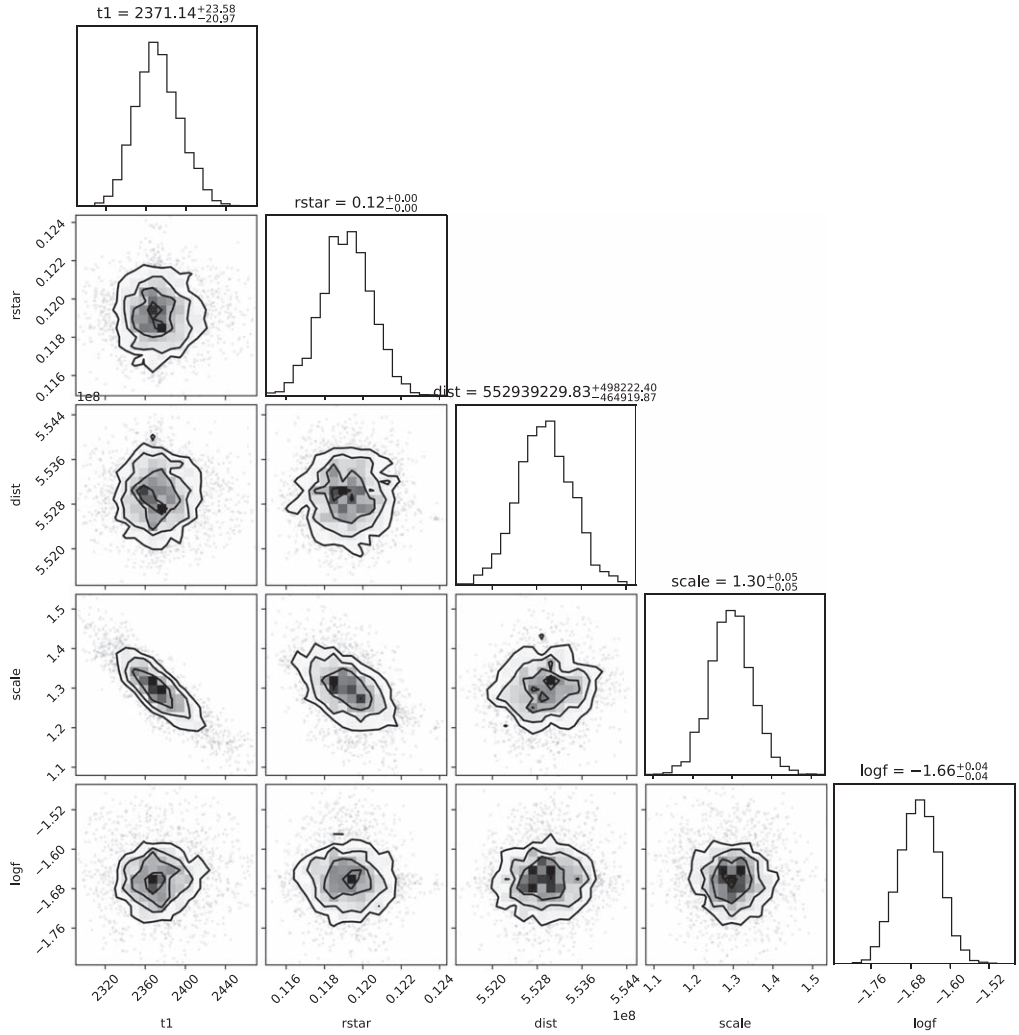

Figure 12. A corner plot of the inferred parameters of the 1-comp model. Here "t1," "rstar," "dist," "scale," and "logf" represent the temperature of the quiescent component, the star's radius, the star's distance, the scaling parameter, and additional noise present in the data, respectively. The model was constructed using the SPHINX spectral grid and NIRSpec data.

ORCID iDs

Fatemeh Davoudi https://orcid.org/0000-0002-1787-3444
Benjamin V. Rackham https://orcid.org/0000-0002-3627-1676
Michaël Gillon https://orcid.org/0000-0003-1462-7739
Julien de Wit https://orcid.org/0000-0003-2415-2191
Adam J. Burgasser https://orcid.org/0000-0002-6523-9536
Laetitia Delrez https://orcid.org/0000-0001-6108-4808
Aishwarya Iyer https://orcid.org/0000-0003-0971-1709
Elsa Ducrot https://orcid.org/0000-0002-7008-6888

References

Agol, E., Dorn, C., Grimm, S. L., et al. 2021, PSJ, 2, 1
Akaike, H. 1998, in Breakthroughs in Statistics. Springer Series in Statistics, ed. S. Kotz & N. L. Johnson (New York: Springer), 610
Albert, L., Lafrenière, D., René, D., et al. 2023, PASP, 135, 075001
Allers, K. N., & Liu, M. C. 2013, ApJ, 772, 79
Astropy Collaboration, Price-Whelan, A. M., Lim, P. L., et al. 2022, ApJ, 935, 167
Astropy Collaboration, Price-Whelan, A. M., Sipőcz, B. M., et al. 2018, AJ, 156, 123
Astropy Collaboration, Robitaille, T. P., Tollerud, E.., et al. 2013, A&A, 558, A33
Astropy-Specutils Development Team, 2019 Specutils: Spectroscopic Analysis and Reduction, Astrophysics Source Code Library, ascl:1902.012
Barnes, J. R., Jenkins, J. S., Jones, H. R. A., et al. 2014, MNRAS, 439, 3094
Bourrier, V., Ehrenreich, D., Wheatley, P. J., et al. 2017, A&A, 599, L3
Brady, M., Bean, J. L., Seifahrt, A., et al. 2023, AJ, 165, 129
Buchner, J. 2021, JOSS, 6, 3001
Burgasser, A. J., Logsdon, S. E., Gagné, J., et al. 2015, ApJS, 220, 18
Burgasser, A. J., & Mamajek, E. E. 2017, ApJ, 845, 110
Burgasser, A. J. & Splat Development Team 2017, in Astronomical Society of India Conf. Ser.. 14, The SpeX Prism Library Analysis Toolkit (SPLAT): A Data Curation Model (Bassi: BASI), 7
Bushouse, H., Eisenhamer, J., Dencheva, N., et al. 2023, JWST Calibration Pipeline, v1.11.4, Zenodo, doi:10.5281/zenodo.8247246
Coulombe, L.-P., Benneke, B., Challener, R., et al. 2023, Natur, 620, 292
Cushing, M. C., Rayner, J. T., Davis, S. P., & Vacca, W. D. 2003, ApJ, 582, 1066
Cushing, M. C., Rayner, J. T., & Vacca, W. D. 2005, ApJ, 623, 1115
Cutri, R. M., et al. 2012, VizieR Online Data Catalog: WISE All-Sky Data Release (Cutri+ 2012), VizieR On-line Data Catalog: II/311, Originally published in: 2012wise.rept....1C
Cutri, R. M., Skrutskie, M. F., van Dyk, S., et al. 2003, 2MASS All Sky Catalog of point sources ("The IRSA 2MASS All-Sky Point Source Catalog, NASA/IPAC Infrared Science Archive.)
Dekker, H., D'Odorico, S., Kaufer, A., Delabre, B., & Kotzlowski, H. 2000, Proc. SPIE, 4008, 534
Delfosse, X., Forveille, T., Ségransan, D., et al. 2000, A&A, 364, 217
Delrez, L., Murray, C. A., Pozuelos, F. J., et al. 2022, A&A, 667, A59

Desort, M., Lagrange, A. M., Galland, F., Udry, S., & Mayor, M. 2007, A&A, 473, 983
Dmitrienko, E. S., & Savanov, I. S. 2018, ARep, 62, 412
Dole, S. H. 1964, Habitable Planets for Man (New York: Blaisdell Pub. Co)
Doyon, R., Willott, C. J., Hutchings, J. B., et al. 2023, PASP, 135, 098001
Ducrot, E., Gillon, M., Delrez, L., et al. 2020, A&A, 640, A112
Dupuy, T. J., & Kraus, A. L. 2013, Sci, 341, 1492
Engle, S. G., & Guinan, E. F. 2011, Red Dwarf Stars: Ages, Rotation, Magnetic Dynamo Activity and the Habitability of Hosted Planets, in ASP Conf. Ser. 451, 9th Pacific Rim Conf. on Stellar Astrophysics, ed. S. Qain et al. (San Francisco, CA: ASP), 285
Feinstein, A. D., Radica, M., Welbanks, L., et al. 2023, Natur, 614, 670
Filippazzo, J. C., Rice, E. L., Faherty, J., et al. 2015, ApJ, 810, 158
Foreman-Mackey, D. 2016, JOSS, 1, 24
Foreman-Mackey, D., Farr, W., Sinha, M., et al. 2019, JOSS, 4, 1864
Foreman-Mackey, D., Hogg, D. W., Lang, D., & Goodman, J. 2013, PASP, 125, 306
Gaia Collaboration, Helmi, A., van Leeuwen, F., et al. 2018, A&A, 616, A12
Gaia Collaboration, Prusti, T., de Bruijne, J. H. J., et al. 2016, A&A, 595, A1
Gaia Collaboration, Vallenari, A., Brown, A. G. A., et al. 2023, A&A, 674, A1
Garcia, L. J., Moran, S. E., Rackham, B. V., et al. 2022, A&A, 665, A19
Gharib-Nezhad, E., Iyer, A. R., Line, M. R., et al. 2021, ApJS, 254, 34
Gharib-Nezhad, E., & Line, M. R. 2019, ApJ, 872, 27
Gillon, M., Jehin, E., Lederer, S. M., et al. 2016, Natur, 533, 221
Gillon, M., Triaud, A. H. M. J., Demory, B.-O., et al. 2017, Natur, 542, 456
Gizis, J. E., Monet, D. G., Reid, I. N., et al. 2000, AJ, 120, 1085
Gonzales, E. C., Faherty, J. K., Gagné, J., et al. 2019, ApJ, 886, 131
Gray, R. O., & Corbally, C. J. 2009, Stellar Spectral Classification (Princeton, NJ: Princeton Univ. Press)
Greene, T. P., Bell, T. J., Ducrot, E., et al. 2023, Natur, 618, 39
Harris, C. R., Millman, K. J., van der Walt, S. J., et al. 2020, Natur, 585, 357
Howell, S. B., Everett, M. E., Horch, E. P., et al. 2016, ApJL, 829, L2
Hunter, J. D. 2007, CSE, 9, 90
Husser, T. O., Wende-von Berg, S., Dreizler, S., et al. 2013, A&A, 553, A6
Iyer, A. R., & Line, M. R. 2020, ApJ, 889, 78
Iyer, A. R., Line, M. R., Muirhead, P. S., Fortney, J. J., & Gharib-Nezhad, E. 2022, The SPHINX M-dwarf Spectral Grid. I. Benchmarking New Model Atmospheres to Derive Fundamental M-Dwarf Properties, v2, Zenodo, doi:10.5281/zenodo.7416042
Iyer, A. R., Line, M. R., Muirhead, P. S., Fortney, J. J., & Gharib-Nezhad, E. 2023, ApJ, 944, 41
Jakobsen, P., Ferruit, P., Alves de Oliveira, C., et al. 2022, A&A, 661, A80
Jeffers, S. V., Schöfer, P., Lamert, A., et al. 2018, A&A, 614, A76
Kirkpatrick, J. D., Cruz, K. L., Barman, T. S., et al. 2008, ApJ, 689, 1295
Kirkpatrick, J. D., Henry, T. J., & Irwin, M. J. 1997, AJ, 113, 1421
Kirkpatrick, J. D., Henry, T. J., & McCarthy, D. W. J. 1991, ApJS, 77, 417
Lee, K.-G., Berger, E., & Knapp, G. R. 2010, ApJ, 708, 1482
Lim, O., Benneke, B., Doyon, R., et al. 2023, ApJL, 955, L22
Long, L., Zhang, L.-Y., Han, X. L., et al. 2018, AJ, 156, 220
Luger, R., Sestovic, M., Kruse, E., et al. 2017, NatAs, 1, 0129
Maas, A. J., Ilin, E., Oshagh, M., et al. 2022, A&A, 668, A111
Mann, A. W., Deacon, N. R., Gaidos, E., et al. 2014, AJ, 147, 160
Marshall, J. L., Burles, S., Thompson, I. B., et al. 2008, Proc. SPIE, 7014, 701454
Morris, B. M., Agol, E., Davenport, J. R. A., & Hawley, S. L. 2018, ApJ, 857, 39
Mullan, D. J., MacDonald, J., Dieterich, S., & Fausey, H. 2018, ApJ, 869, 149
Narrett, I. S., Rackham, B. V., & de Wit, J. 2024, AJ, 167, 107
Niraula, P., de Wit, J., Gordon, I. E., Hargreaves, R. J., & Sousa-Silva, C. 2023, ApJL, 950, L17
Niraula, P., de Wit, J., Gordon, I. E., et al. 2022, NatAs, 6, 1287
Paudel, R. R., Gizis, J. E., Mullan, D. J., et al. 2018, ApJ, 858, 55
Paudel, R. R., Gizis, J. E., Mullan, D. J., et al. 2019, MNRAS, 486, 1438
Polyansky, O. L., Kyuberis, A. A., Zobov, N. F., et al. 2018, MNRAS, 480, 2597
Pont, F., Knutson, H., Gilliland, R. L., Moutou, C., & Charbonneau, D. 2008, MNRAS, 385, 109
Rackham, 2023 speclib (0.0-beta.0). Zenodo, doi:10.5281/zenodo.7868050
Rackham, B., Espinoza, N., Apai, D., et al. 2017, ApJ, 834, 151
Rackham, B. V., Apai, D., & Giampapa, M. S. 2018, ApJ, 853, 122
Rackham, B. V., Apai, D., & Giampapa, M. S. 2019, AJ, 157, 96
Rackham, B. V., & de Wit, J. 2023, arXiv:2303.15418
Rackham, B. V., Espinoza, N., Berdyugina, S. V., et al. 2023, RASTI, 2, 148
Radica, M., Welbanks, L., Espinoza, N., et al. 2023, MNRAS, 524, 835
Rayner, J. T., Cushing, M. C., & Vacca, W. D. 2009, ApJS, 185, 289
Rayner, J. T., Toomey, D. W., Onaka, P. M., et al. 2003, PASP, 115, 362
Reid, I. N., & Hawley, S. L. 2000, New Light on Dark Stars. Red dwarfs, low-mass stars, brown dwarfs (London: Springer)
Reid, I. N., & Hawley, S. L. 2005, New Light on Dark Stars : Red dwarfs, low-mass stars, brown dwarfs (London: Springer)
Reiners, A., & Basri, G. 2010, ApJ, 710, 924
Roettenbacher, R. M., & Kane, S. R. 2017, ApJ, 851, 77
Rojas-Ayala, B., Covey, K. R., Muirhead, P. S., & Lloyd, J. P. 2010, ApJL, 720, L113
Rojas-Ayala, B., Covey, K. R., Muirhead, P. S., & Lloyd, J. P. 2012, ApJ, 748, 93
Schneider, A. C., Greco, J., Cushing, M. C., et al. 2016, ApJ, 817, 112
Schöfer, P., Jeffers, S. V., Reiners, A., et al. 2019, A&A, 623, A44
Shulyak, D., Reiners, A., Engeln, A., et al. 2017, NatAs, 1, 0184
Stassun, K. G., Collins, K. A., & Gaudi, B. S. 2017, AJ, 153, 136
Stassun, K. G., & Torres, G. 2016, AJ, 152, 180
Su, T., Zhang, L.-y., Long, L., et al. 2022, ApJS, 261, 26
Vacca, W. D., Cushing, M. C., & Rayner, J. T. 2003, PASP, 115, 389
Van Grootel, V., Fernandes, C. S., Gillon, M., et al. 2018, ApJ, 853, 30
Vida, K., Kővári, Z., Pál, A., Oláh, K., & Kriskovics, L. 2017, ApJ, 841, 124
Wagenmakers, E., & Farrell, S. 2004, Psychonomic Bulletin & Review, 11, 192
Wakeford, H. R., Lewis, N. K., Fowler, J., et al. 2019, AJ, 157, 11
West, A. A., & Hawley, S. L. 2008, PASP, 120, 1161
West, A. A., Hawley, S. L., Walkowicz, L. M., et al. 2004, AJ, 128, 426
Wheatley, P. J., Louden, T., Bourrier, V., Ehrenreich, D., & Gillon, M. 2017, MNRAS, 465, L74
Zhang, Z., Zhou, Y., Rackham, B. V., & Apai, D. 2018, AJ, 156, 178